Can Airborne Ground Penetrating Radars Explore Groundwater in Hyper-Arid Regions?

ROBERT M. BEAUCHAMP[1], DARMINDRA D. ARUMUGAM[1],
MARIKO S. BURGIN[1], (Senior Member, IEEE), JACK D. BUSH[1],
ALA KHAZENDAR[1], YONGGYU GIM[1], SULTAN ALMORQI[2],
MAJED ALMALKI[2], YASIR A. ALMUTAIRI[2], ALI A. ALSAMA[2],
AND ABDULRAHMAN G. ALANEZI[2]

[1] Jet Propulsion Laboratory, California Institute of Technology, Pasadena, CA 91109, USA
[2] King Abdulaziz City for Science and Technology, Riyadh 12371, Saudi Arabia

Corresponding author: Robert M. Beauchamp (robert.m.beauchamp@jpl.nasa.gov)

ABSTRACT Groundwater provides roughly 43% of the water used globally for irrigated agriculture. Understanding, predicting, and managing the environmental processes that define the natural capital of Earth's changing groundwater is one of the most pressing societal challenges of the 21st century. To understand the influence of the dynamics in the vadose zone on terrestrial ecosystems, and to estimate the future sustainability of groundwater resources, a regional and eventually global assessment of water table depth is required. To enable observations of the hydrologic systems' dynamics, the feasibility of an airborne ground penetrating radar (GPR) system is considered as a first step to effectively provide both large spatial coverage and short revisit times. Such a capability has the potential to enable large-scale surveys to directly observe the shallow subsurface hydrologic processes. To evaluate the capabilities of such a system, we start with a review of soil and subsurface material properties, with a focus on hyper-arid regions. Using first principles, results from literature reviews, and recent field measurements, we then investigate the effects of attenuation and surface clutter to identify the potential capabilities and challenges of an airborne GPR to investigate the spatio-temporal dynamics of the vadose zone. In this paper, we arrive at a qualified "yes" as an answer the title's question. With low radar frequencies (on the order of 10 MHz or less), adequate ground clutter rejection, and medium or higher vadose zone soil resistivity, the detection of water table depths of 50 m and beyond are feasible.

INDEX TERMS Airborne radar, ground penetrating radar, remote monitoring, water resources, hydrology, soil.

I. INTRODUCTION

The top of the water table is an undulating surface between oxygenated soils and water-saturated aquifers. The water tables' top can be at or above the soils' surface (in the case of lakes and rivers) to depths potentially hundreds of meters below the surface. The vadose zone, or unstaturated zone, is the region between the Earth's surface and the top of the water table. A globally-averaged water table depth is approximated to be 5 meters [1]. Groundwater provides roughly 43% of the water used globally for irrigated agriculture [2]. This constant demand, in addition to a projected human population increase to 9 billion by 2050, is expected to increase the need for clean drinking water by over 50% in the coming decades [3], [4]. Understanding, predicting, and managing the environmental processes that define the natural capital

of Earth's changing groundwater is one of the most pressing societal challenges of the 21st century [5].

An analysis of groundwater in the first 2 km of the Earth's crust indicates that less than 6% of available groundwater is less than 50 years old [6]. This suggests that recharge times of deep aquifers can be on the order of decades, centuries, or longer. The increased demand for water resources around the world and the associated accelerated exploitation of these deep aquifers in the last century is driving the need to understand the hydrology and dynamics of such systems and to monitor and manage our water resources. The hydrological response of the subsurface to precipitation, infiltration, and evapotranspiration is an important part of the water budget for any region. By tracking tracer material infiltration in the vadose zone, the hydrological timescales of the unsaturated,

R. M. Beauchamp *et al.*: Can Airborne GPRs Explore Groundwater in Hyper-Arid Regions?

IEEE*Access*

near-surface depths are reported to be as shorts as hours [7] to days [8]. From measurements of hydraulic conductivity in near surface aquifers (such as unconfined aquifers which constitute the water table), the recharge times are estimated to be on the order of days to months [8]–[11].

To understand the influence of the dynamics in the vadose zone on terrestrial ecosystems and to estimate the future sustainability of groundwater resources, a regional and eventually global assessment of the water table depth is required. Root-zone soil moisture and the moisture in the vadose zone (soils between the Earth's surface and the top of the water table) is an important link in understanding the water cycle that is largely missing in current observational systems.

Existing spaceborne observations of soil moisture have been made mostly at L-band and higher frequencies and are limited to penetration depths of a few centimeters [12]. These surface soil moisture measurements are subject to high variability from precipitation and diurnal temperature cycles. Similarly, regional and global scale measurements of changes in available water have been inferred from surface deformation and gravity measurements [8], [13]. These techniques can measure changes in the integrated water volume at regional scales and typically resolve monthly or seasonal scale variations in water storage. With the addition of direct observations of the vadose zone depth and saturation, the spatial and temporal dynamics linking precipitation and available surface water with groundwater recharge and storage can be more effectively modeled.

Surface-based ground-penetrating radar (GPR) has enabled imaging of the near-surface features, including hydrological features. Surface-based measurements are typically limited to small areas due to the labor intensive nature of collecting observations. With an airborne radar sounder, large regions could be surveyed with high spatial (and temporal) resolution. The availability of high spatial and temporal resolution surveys enables new insight into the near-surface hydrologic systems and supplements other data sources. For a radar-based exploration of groundwater, the distribution of water near the surface (potentially to depths of hundreds of meters) is the primary motivating goal.

This paper presents an initial investigation into the technical challenges and capabilities of airborne sounding radar concepts with applications to aquifer detection in hyper-arid regions. This work intends to elucidate the likelihood of subsurface feature detection (specifically, the top of the water table) for such an application. Theoretical, experimental, and simulation results are used to quantify performance and to identify areas of technical risk. This work discusses capabilities and associated technology requirements (and limitations) to achieve radar sounding at sufficient depths to detect water in arid desert regions.

To evaluate the performance of a notional airborne radar system, an electrical model of the subsurface material and its morphological structure is required. While numerous field experiments and characterizations of soil properties are reported in the literature, it is clear that the electromagnetic

properties of the subsurface are highly variable and sensitive to localized conditions. As such, the approach in this work has been to consider a parameter space to understand the design and performance sensitivity to material (and system) properties. A generalized discussion of the attenuation and scattering characteristics is presented using numerous examples of soil measurements from the literature [Sections II and III]. The effects of surface clutter on an airborne radar are evaluated in detail [Section IV]. Combined with an analysis of field experiments [Section V] and a review of current sounding radars [Section VI], the characteristics of an airborne desert radar sounder are discussed. Within this framework, we present a first-order evaluation of the capabilities of an airborne sounder to detect subsurface aquifers (specifically, the top of the water table). The functional characteristics and technical trade-offs for an airborne radar sounder system are discussed [Section VII].

II. HYDROLOGY

A sounding radar's performance is dependent on the attenuation of its signal within the subsurface. Attenuation, which limits the radar's detection depth, can vary significantly with changes in the water saturation of the material. It is worth noting that changes in the subsurface composition, including gradients in the water content, will scatter the radar's signal; it is the intention for the radar to subsequently detect this signal. The distribution of the water gradients, assuming a homogeneous soil medium, will be briefly considered in the following paragraphs. An analysis of the material properties as they impact electrical and hydrologic characteristics will provide insight into the radar's capabilities to penetrate the subsurface and detect subsurface features.

Water saturation, S_w, is the fraction of available pore space that contains water. The available pore space or the material's porosity, ϕ, is the volume fraction not occupied by solid soil grains (e.g, it is a measure of the space between the particles). Note that saturated materials (i.e., $S_w = 1$) with two different porosities will have different water volumes within the pore space (the saturated water content). For $0 < S_w < 1$, the pore space is a mixture of air and water. The region (depth) of unsaturated material is referred to as the vadose zone. Water content is typically reported in terms of the volume fraction or water saturation (which are related by ϕ).

For naturally occurring soils, there is a minimum water saturation within the soil that is driven by the surface tension and electrostatic binding of water to soil particles for a given pressure gradient. Drying affects (evaporation) can reduce the soil moisture below this limit but it typically only impacts the surface layer of soil [14], [15]. Long periods of drought and intense surface heating will vary the transition depth, but for the purposes of deep radar sounding these can largely be neglected as they are only expected to be significant within the first meter of the surface.

The evaporation rates from water in local river sand was compared to that of free standing water in South West Africa [14]. Materials with different ratios of particle sizes

IEEE *Access*

R. M. Beauchamp *et al.*: Can Airborne GPRs Explore Groundwater in Hyper-Arid Regions?

TABLE 1. Water and material properties for sandy soils in China (Adapted from [18]).

Geographic Zone	Climatic Zone	Porosity (%)	Capillary rise height (m)	Depth of Water Table (m)
Taklimakan desert	Hyperarid	46	0.53	4.5
Hexi Corridor	Arid	38.95	0.52	2-3
Alxa sandy land	Arid	43.7	0.50	4
Mu Us desert	Arid	41.5	0.55	4
Yanchi	Semiarid	44.23	0.75	3.8
Alluvium Yellow River	Semihumid	43.4	0.73	2.5
Alluvium Yellow River	Semihumid	45.1	0.52	3.5
Horqin sandy land	Semihumid	35.37	0.65	3
Hebei sandy land	Semihumid	44.7	0.60	2.7
Nanchang eolian sandy land	Subtropical humid	39.69	0.57	3

were compared to evaluate the impact of grain size on evaporation. The water table depth was kept constant within the material during testing to characterize the evaporation rates. For sand with a mean grain diameter of 0.32 mm and a 30 cm water table depth, the evaporation rate was 50% of the rate of an open water surface. For sand with a mean grain diameter of 0.53 mm, the evaporation rate is approximately 25% of the open surface rate. (This indicates that the capillary rise is reduced with larger grain diameters, hence less water migrates toward the surface.) If the depth to the water table was changed to 60 cm (still with a mean grain diameter of 0.53 mm), the evaporation rate reduced to 10% of an open water surface. For water saturated sand (the water table level is at the sand's surface), the evaporation rate is 8% higher than that of standing water. This increase was attributed to the additional heat retention in the saturated sand which enhances evaporation [14]. As one might expect, the evaporation rate at the surface is a function of ambient conditions.

In the hyper-arid, southwestern region of Saudi Arabia (specifically, at 22° 08′ 7.50″ N, 39° 16′ 17.35″ E) the evaporation extinction depth in sand dunes was measured as part of a larger effort to consider using dunes as aquifer storage systems in the region [16]. The soil porosity was measured as $\phi = 0.33, 0.40$, and 0.41 for three different samples (the authors compare their results to another study [17], which found the mean porosity of 50 samples to be $\phi = 0.39 \pm 0.02$ for the same dunes). A diurnal temperature variation exhibited fluctuations of 10-20°C in the first 10 cm of depth. The temperature variation reduced to 3-7°C between depths of 12 and 35 cm. A diurnal variation in soil water content was observed in the top 12 cm of the subsurface depth, and the water saturation gradient stabilized at a depth of approximately 1 m.

For sandy areas in China with hyper-arid to subtropical-humid climates, a subset of relevant results regarding the climatology, groundwater characteristics, and soil properties are summarized in Table 1 [18]. The reported measurements of the capillary rise height in "dry" sandy soils for these different climates is between 0.5 and 0.75 meters. The water table depths were measured to be between 2 and 4.5 meters below ground level.

At a test site in Lachenaie, Canada (near Montreal), the capillary rise height was estimated to be 0.3 m for sand

with a "dry" water saturation fraction of approximately $S_w = 0.1$ [19]. The surface layer consists of medium-to-coarse sand with a 60th percentile diameter of 0.71 mm. At this site, the water table (i.e., 100% saturation) was measured at a depth of 1.9 m.

A model for the hydrostatic distribution of pore water in a porous material [20] is used to estimate the transition depth from a "dry" saturation state to a water saturated state. The saturation fraction S_w for a given height, h, above the fully saturated point ($S_w = 1$ at $h = 0$) is

$$S_w = e^{-\lambda_p h} \tag{1}$$

where λ_p is the pore constant of the homogeneous soil. Using Eqn. 1 and the pore constant for a sampling of representative materials in Table 2, the capillary rise height above the water table can be calculated. We assume that the material has a minimum saturation of approximately $S_w = 0.1$ to estimate the capillary rise heights. Figure 1 shows the exponential model's estimated water saturation as a function of height above the water table and Table 2 includes estimates of the transition height from dry to fully saturated.

TABLE 2. Model estimates of transition lengths from "dry" ($S_w = 0.1$) to water-saturated ($S_w = 1.0$) for various materials. (Adapted from [20].)

Type	λ_p	S_w =10%-100% Length (m)
Fine sand	3.7	0.62
Volcanic sand	2.29	1.01
Berea sandstone	3.69	0.62
Fragmented mixture	2.89	0.80
Hygiene sandstone	4.17	0.55

While this discussion is an over-simplification of the dynamics of hydrological processes in soils, it does provide approximate characteristics relevant to modeling the electromagnetic response of soils for low frequency GPR (up to tens of MHz). In the absence of evaporation or infiltration (i.e., no precipitation), an exponential gradient in the water saturation as a function of height above the water table is observed from the point of saturation ($S_w = 1$) to a minimum saturation fraction; it is largely a function of soil structure under hydrostatic and isobaric conditions. Without any pressure gradients in the subsurface, the saturation is due
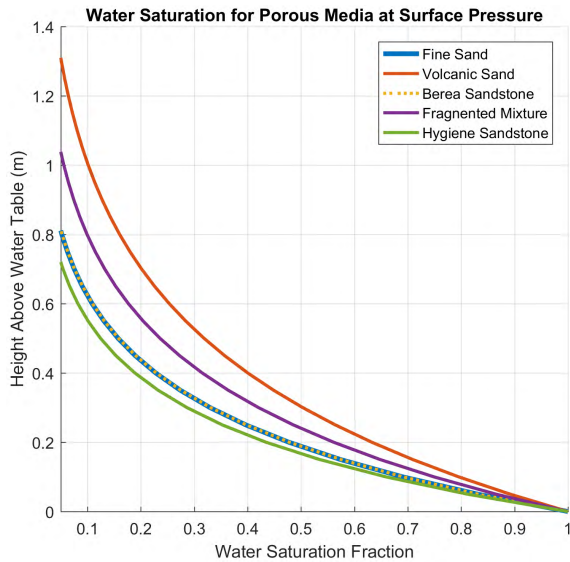
R. M. Beauchamp et al.: Can Airborne GPRs Explore Groundwater in Hyper-Arid Regions?

IEEE *Access*

FIGURE 1. Modeled water saturation fraction as a function of height above the water table for various materials.

to capillary pressure (the surface tension) of the water and soil particles. Larger diameter particles will lead to lower bulk capillary pressure and therefore a smaller transition zone (and potentially a lower minimum S_w). From the available measurements and models, the capillary transition zone is expected to be between 0.5 and 1 meters for sandy areas. At depths below this transition zone, the material is water saturated. Above the transition zone, the material's minimum saturation is limited by the bound water (due to surface tension) within the soils grain structure. Fine grain material will have a higher minimum S_w than coarse grain materials. For depths close to the surface (down to approximately one meter), surface heating drives the evaporation of the bound pore fluid and thus further reduces the soil moisture toward zero.

III. ELECTROMAGNETIC THEORY

For the following discussion it is assumed that the magnetic permeability μ is that of free space ($\mu_0 = 4\pi \cdot 10^{-7}$ H/m). This is in good agreement with the electromagnetic properties of the typical subsurface materials expected throughout the regions where an airborne radar sounder is expected to operate [21]. The dielectric permittivity is a complex-valued quantity

$$\epsilon = \epsilon' - j\epsilon'' \qquad (2)$$

where $j = \sqrt{-1}$. The permittivity is sometimes referenced in terms of the relative permittivity scale factor ϵ_r, which defines the real part of the permittivity as

$$\epsilon' = \epsilon_0 \epsilon_r, \qquad (3)$$

where the permittivity of free space is $\epsilon_0 = 8.854 \cdot 10^{-12}$ F/m. Note, that ϵ_r is a unit-less scale factor ≥ 1.

The propagation constant of an electromagnetic wave propagating within a general medium is

$$\gamma = \alpha + j\beta = j\omega\sqrt{\mu\epsilon}\sqrt{1 - j\frac{\sigma_c}{\omega\epsilon}} \qquad (4)$$

where σ_c is the electrical conductivity. The "c" subscript is needed to differentiate it from radar cross-section (RCS), which is discussed later. The wavelength within the medium is $\lambda = 2\pi/\beta$, which is related to the propagation speed, and the attenuation (loss) within the medium is determined by α.

A forward propagating plane wave's electric field is described by

$$E(z) = E_0 e^{-\gamma z} \qquad (5)$$

where E_0 is the initial electric field amplitude and z is the one-way propagation distance. The propagation constant can be separated into the loss and velocity components as

$$E(z) = E_0 e^{-\alpha z} e^{-j\beta z}. \qquad (6)$$

Here, the reduction in the electric field is due to absorption loss (α) assuming a plane wave. (Recall, $e^{-j\beta z}$ only affects the signal's phase and has a magnitude of 1.) This equation does not account for spherical fading or scattering losses from within the medium. The one-way specific attenuation due to absorption (which assume $z = 1$) is calculated as

$$A_1 = -20\log_{10}\left(e^{-\alpha}\right) = 8.686\alpha \qquad (7)$$

with units of decibels per meter. The negative sign before the $20\log_{10}$ is to ensure that the one-way specific attenuation A_1 is non-negative. (Note, A_1 is a loss, which by convention is subtracted, reducing the signal power.) It is important to note that this is a one-way attenuation. For monostatic radar applications, the signal must propagate through the material twice, effectively doubling the distance the wave travels and therefore doubling the total signal attenuation (i.e., a two-way loss, A_2).

The signal attenuation due to only absorption is a function of the material's properties and can be calculated as [22]

$$\alpha = \omega\left[\frac{\epsilon'\mu}{2}\left(\sqrt{1 + \tan^2\delta} - 1\right)\right]^{1/2} \qquad (8)$$

with units of Np/m. The loss tangent is simply

$$\tan\delta = \frac{\epsilon''}{\epsilon'}. \qquad (9)$$

The permittivity can also be rewritten in terms of the relative permittivity and the loss tangent

$$\epsilon = \epsilon_r \epsilon_0 (1 - j\tan\delta). \qquad (10)$$

From Eqns. 4 and 9, the loss within a material can be due to conduction loss σ_c and dielectric losses ϵ''. For a general lossy material, both the conduction losses and dielectric losses can be represented by the effective loss tangent

$$\widetilde{\tan\delta} = \frac{\omega\epsilon'' + \sigma_c}{\omega\epsilon'}. \qquad (11)$$

IEEE *Access*

R. M. Beauchamp *et al.*: Can Airborne GPRs Explore Groundwater in Hyper-Arid Regions?

It is easily seen that the dielectric loss and conduction loss can be combined for a fixed frequency. The conduction is independent of frequency. If the dielectric relaxation losses (due to $\omega\epsilon''$) are small with respect to the conduction loss (i.e., $\omega\epsilon'' \ll \sigma_c$), then the conduction loss dominates the loss tangent. For soils and typical GPR frequencies this is a good assumption [23]. For materials with high conductivities (or for electromagnetic waves at low frequencies) the material may be classified as a "good conductor". A good conductor is characterized by $\sigma_c \gg \omega\epsilon'$, which leads to an approximation of the loss factor

$$\alpha \approx \sqrt{\frac{\omega\mu\sigma_c}{2}}. \tag{12}$$

From review of Eqn. 12 it is noted that in the good conductor regime the attenuation due to absorption varies as a function of $\sqrt{f}$. Therefore, if the material's properties are constant for all frequencies, decreasing the frequency by a factor of 10 will reduce the specific attenuation (in decibels) by a factor of 3.16. Note that this assumption may not be true for large changes in the frequency ratio, as the electromagnetic properties of the soil and pore fluid materials can exhibit a strong frequency dependence [23], [24]. In Fig. 2, the attenuation in a homogeneous medium is considered for a range of frequencies. For this example, a constant permittivity of $\epsilon_r = 10$ was selected (this is in the range of typical permittivities for soils partially saturated with water). The range of conductivities are representative of subsurface soils with varying water content and salinity. The significance of
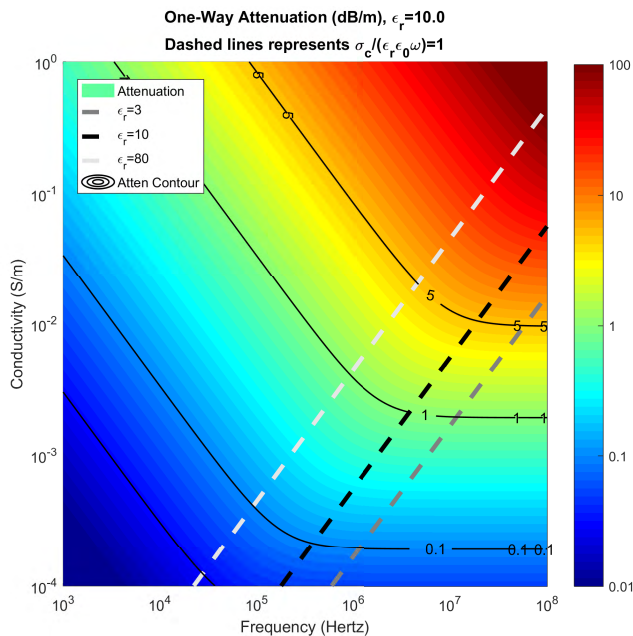

FIGURE 2. One-way specific attenuation (due to absorption) versus frequency for a relative permittivity of $\epsilon_r = 10$. Attenuation contours are provided for reference. The dashed lines are the points where $\sigma_c/(\epsilon'\omega) = 1$ to indicate the approximate transition from dominating conduction losses to significant dielectric losses. The transitions for $\epsilon_r = 3$ and $\epsilon_r = 80$ are provided for reference to indicate how changes in permittivity affect the good conductor assumption.
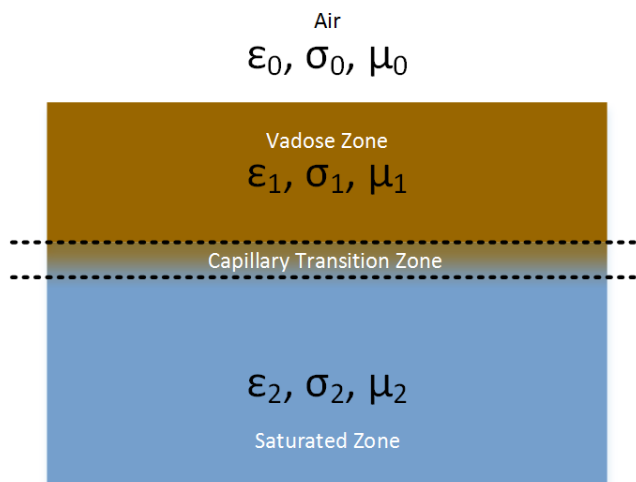
conduction losses and dielectric losses as the frequency varies is observed as an inflection of the specific attenuation. For reference, the approximate boundaries delineating a good conductor from a general lossy material are shown as dashed lines. Note that the specific attenuation is for $\epsilon_r = 10$ but the effect of permittivity changes can be inferred from the two other dashed lines representing $\epsilon_r = 3$ (approximating dry sand) and $\epsilon_r = 80$ (approximating fresh water).

Up to this point, we only considered the relation of the material properties to the attenuation of a propagating signal. From Eqn. 4, it is clear that the propagation speed of the wave is also affected by the medium's properties. The propagation speed (the speed of light in the medium) is

$$v = c = \omega/\beta \tag{13}$$

where

$$\beta = \omega\left[\frac{\epsilon'\mu}{2}\left(\sqrt{1+\tan^2\delta}+1\right)\right]^{1/2}. \tag{14}$$

The conductivity and relative permittivity both affect the wave's propagation speed. Any relative permittivity > 1 will result in a wave speed less than that of free space. As a byproduct, this results in an increased range resolution in the subsurface material compared to that of free space. As one would expect, accurately accounting for the wave speed is necessary to estimate subsurface depths. Techniques are available for ground-based GPR systems to try to estimate the medium's velocity using different observation geometries and measuring the round trip time of the echoes [21], [25]. For materials that are "good conductors", the propagation velocity exhibits a $\sqrt{f}$ dependence.

The suitability of an electromagnetic wave to resolve physical features depends on the wavelength. The wavelength within the medium is also determined by the speed of light $\lambda = 2\pi/\beta$. Features much smaller than a wavelength cannot be distinguished from one another (Rayleigh limit). For features that are sufficiently resolved by the Rayleigh criterion, the range resolution is determined by the received signal bandwidth B. The range resolution of a given waveform (typically determined by the half-power bandwidth) is

$$\Delta R = \frac{c}{2B}. \tag{15}$$

The attenuation is frequency dependent varying as $\sqrt{f}$ (assuming a good conductor $\sigma_c \gg \omega\epsilon$ with constant permittivity). While decreasing the radar's operating frequency improves the maximum penetration depth, these lower frequencies reduce the radar's capability to resolve subsurface features. For a radar's received bandwidth of 1 MHz with a material permittivity of $\epsilon_r = 20$ and negligible conductivity, the subsurface resolution from Eqn. 15 is $300/(2\sqrt{20}) = 33.5$ m.

A. RADAR CROSS-SECTION

In its simplest form, the subsurface can be approximated as vertically varying layers, where each layer is of homogeneous

R. M. Beauchamp *et al.*: Can Airborne GPRs Explore Groundwater in Hyper-Arid Regions?

IEEE *Access*

Air

$$\varepsilon_0, \sigma_0, \mu_0$$

Vadose Zone

$$\varepsilon_1, \sigma_1, \mu_1$$

Capillary Transition Zone

$$\varepsilon_2, \sigma_2, \mu_2$$

Saturated Zone

FIGURE 3. Conceptual three-layered model of an airborne sounding radar for detection of subsurface water. All layers can be assumed homogeneous (with exception of the capillary transition zone). The vadose zone can be approximated as a partially saturated "dry" region.

composition. Figure 3 illustrates the idealized sounder case with three material layers. The top layer is air, the middle layer is the "dry" vadose zone, which transitions to the water-saturated layer on the bottom. The capillary transition zone is illustrated between the saturated layer and the vadose zone layer. When the wavelength is large with respect to the depth of the capillary zone, the interface gradient can be approximated as a step change between two homogeneous dielectrics. The wave impedance of a material is determined by its electromagnetic properties as

$$\eta = \frac{j\omega\mu}{\gamma}. \tag{16}$$

For a first order analysis, the vertical sounding radar's signal can be approximated by a plane-wave that is perpendicularly incident at the surface and the subsequent subsurface layers. For this plane wave, the change in impedance between the two materials results in a fraction of the incident field to be reflected and the remaining power to be transmitted. The fraction of the field that is reflected is determined by the reflection coefficient

$$\Gamma = \frac{\eta_2 - \eta_1}{\eta_2 + \eta_1}. \tag{17}$$

The transmission coefficient can be similarly calculated (for a perpendicular incidence) as

$$T = \frac{2\eta_2}{\eta_2 + \eta_1}. \tag{18}$$

The ratio of the incident power to the scattered power of an object is characterized by its radar cross-section (RCS) defined as

$$\sigma = 4\pi R \frac{P_s}{P_i} \underset{R\to\infty}{} \tag{19}$$

where the RCS's units are in m^2. When the incident and scattered direction are not the same, the radar cross-section is referred to as a bistatic RCS. When the incident and scattered directions are the same, it is referred to as the monostatic RCS or backscattered RCS. The total scattering RCS (σ_s) is the sum of all power scattered by the object.

The plane wave's electric field is related to its power by

$$P = \frac{|E|^2}{2\eta}. \tag{20}$$

If we consider the incident, reflected, and transmitted fields separately (not coincident in the same space and time), then the electric and magnetic field are related only by a real-valued impedance. The time-averaged power flux through a unit area is

$$P = \frac{1}{2}Re\left\{E \times H^*\right\} = \frac{|E|^2}{2Re\left\{\eta\right\}} \tag{21}$$

with units of W/m^2. If we assume an incident plane wave with amplitude E_0 at the interface with reflection coefficient Γ that then propagates a distance z into a lossy medium, the forward propagating power can be given as

$$P^+(z) = \frac{|E_0|^2\left(1 - |\Gamma|^2\right)}{2Re\left\{\eta\right\}}e^{-2\alpha z}. \tag{22}$$

The "2" in $e^{-2\alpha z}$ accounts for power (since the electric field's magnitude is squared). For a propagating wave with electric field E^+ at the interface, the power density incident on the surface is

$$P_i = \frac{|E^+|^2}{Re\left\{\eta_0\right\}}. \tag{23}$$

Similarly, the power density reflected from the surface for the same incident wave is

$$P_r = \frac{|\Gamma_{ab}|^2|E^+|^2}{Re\left\{\eta_i\right\}} \tag{24}$$

where the subscript "ab" of Γ indicates the interface from material "a" to material "b". Similarly, the wave impedance subscript stands for the incident wave's material "a". Following the RCS definition (we assume far-field powers and therefore drop range from the equation), we can write

$$\sigma = 4\pi \frac{P_r}{P_i}. \tag{25}$$

If the plane wave is reflected off a sufficiently small area (A_s) such that all power is reflected coherently, the surface's RCS can be estimated by

$$\sigma = 4\pi|\Gamma|^2\frac{A_s^2}{\lambda^2}. \tag{26}$$

When considering surface scattering, the surface radar cross-section is typically represented using the RCS per unit area, which is referred to as the normalized radar cross-section (NRCS). The NRCS is a unit-less scale factor (typically presented in decibels). Assuming coherence is maintained over a 1 m^2 area, the NRCS can be calculated as

$$\sigma^0 = \frac{4\pi|\Gamma|^2}{\lambda^2}. \tag{27}$$

IEEE *Access*

R. M. Beauchamp *et al.*: Can Airborne GPRs Explore Groundwater in Hyper-Arid Regions?

It is important to note that this is an approximation of the NRCS (Equation 27) which assumes a coherent reflection over a 1 m area. Typically the NRCS is determined by the scattering response over a larger area where both coherent and incoherent scattering may exist. The reflection coefficient-based estimate of NRCS assumes that $A \ll \lambda^2$. Typically, the radar observed NRCS is made with $A \gg \lambda^2$. (The coherent RCS scales by A^2 while the incoherent RCS scales by A.) The surface morphology (and therefore the coherence of the surface over the radar illuminated area) must be considered. We will see that this coherence function is area and look-angle dependent. With these fundamental assumptions understood, the NRCS calculated from the reflection coefficient can be used with a coherent surface scattering model and suitable model for the surface topography to accurately estimate the radar's observed surface RCS. Such a model is the focus of the Section IV.

The previous discussion considers a perpendicular incident plane wave. For off-perpendicular incidence ($\theta \neq 0$), the propagation direction of the transmitted wave changes due to refraction at the interface and is dependent on the polarization of the electric field. The polarization of the electric field affects the transmission and reflection coefficients (whether the field is parallel to the interface or has a component that is perpendicular to the interface). Consider Fig. 4 which illustrates the incidence, reflection, and transmission angles. Note that the orientations of the polarization vectors are in the plane perpendicular to the propagation direction (here shown for the incident field). The parallel and perpendicular fields are determined with respect to the material interface. From Snell's law, we know that the incidence angle is the angle of

FIGURE 4. Diagram of the incident, transmitted, and reflected electric field directions at the interface between two media with different electromagnetic properties. For non-zero incidence angles, the effects of refraction are observed in the direction of the transmitted fields. Note that the electric field's polarization affects the reflection and transmission coefficients.

reflection ($\theta_i = \theta_r$) and that the ratio of the wavenumbers in the two media are proportional to the ratio of the sine of the angles (i.e., $k_2/k_1 = \sin(\theta_i)/\sin(\theta_t)$, where k_1 is the incident medium).

Consider the reflection coefficient as a function of incidence angle for parallel polarization as

$$\Gamma_\parallel = \frac{\eta_2 \cos \theta_t - \eta_1 \cos \theta_i}{\eta_2 \cos \theta_t + \eta_1 \cos \theta_i}. \tag{28}$$

Similarly, the transmission coefficient for parallel polarization is

$$T_\parallel = \frac{2\eta_2 \cos \theta_i}{\eta_2 \cos \theta_t + \eta_1 \cos \theta_i}. \tag{29}$$

For perpendicularly polarized fields, the reflection coefficient is

$$\Gamma_\perp = \frac{\eta_2 \cos \theta_i - \eta_1 \cos \theta_t}{\eta_2 \cos \theta_i + \eta_1 \cos \theta_t}, \tag{30}$$

and the transmission coefficient for perpendicular polarization is

$$T_\perp = \frac{2\eta_2 \cos \theta_i}{\eta_2 \cos \theta_i + \eta_1 \cos \theta_t}. \tag{31}$$

In Section II, the capillary rise transition zone was discussed and it was shown that the depth of the transition zone from 100% saturation (i.e., the water table at $S_w = 1$) to a saturation of $S_w = 0.1$ (a plausible vadose zone saturation) is typically less than 1 meter. If the radar's wavelength is much greater than the transition depth, the scattering along the impedance gradient is in-phase and adds coherently. This allows us to simplify the estimate of the scattering cross-section to using a simple two layer dielectric contrast model (see Eqns. 17 and 27).

To demonstrate the range of estimated NRCS for the surface and subsurface interfaces, we consider the permittivity, conductivity, and moisture for "high loss soils" from Avra Valley, Arizona at a frequency of 10 MHz as reported by [26]. To estimate the soil moisture fraction it is assumed that $S_w = 1$ when the reported moisture content is 45.5%. The data are fit to a log-linear curve for both conductivity and permittivity to use our model for analysis. The data and model are presented in Fig. 5 and show acceptable agreement with one another for the purposes of evaluating the range of NRCS at the interface between soils with two different water saturation fractions.

To estimate the NRCS of the material, we assume a coherent 1 m^2 patch with perpendicular incidence at the interface (Eqn. 27). For the purposes of estimating the NRCS, the wavelength in the incident material is used. A two layer model for the surface (air-soil interface) and subsurface (partially saturated soil to saturated soil) is used to investigate the relative RCSs of the two interfaces. Again, using a conservative approximation, the wavelength (in the material with the highest effective dielectric constant) should be long with respect to the transition depth to ensure our assumptions hold. (As the length of the interface's saturation gradient
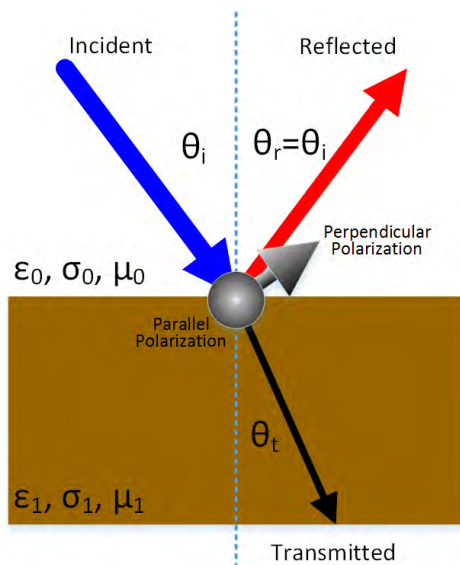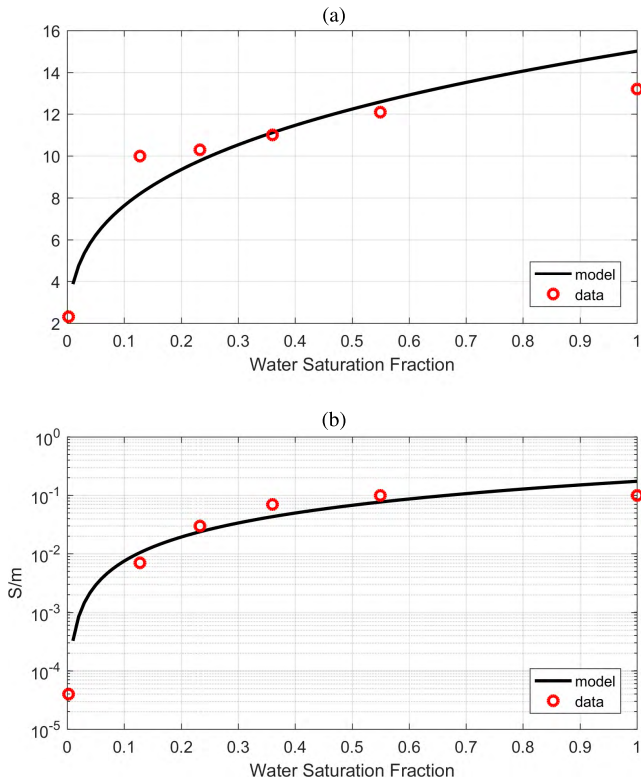
R. M. Beauchamp *et al.*: Can Airborne GPRs Explore Groundwater in Hyper-Arid Regions?

IEEE *Access*

FIGURE 5. Modeled (a) relative permittivity, ϵ_r, and (b) conductivity, σ_c, as a function of water saturation fraction for a "high loss soil" from Avra Valley, AZ. Data at 10 MHz from [26] are shown as red circles and a model fit to the data is shown as a black line.

FIGURE 6. The NRCS (see Equation 27) as a function of frequency is shown for the Avra Valley's high loss soil with different water saturation fractions for the vadose zone. A two layer interface is assumed with a coherent plane wave. The surface (air to partially saturated soil) NRCS is shown in Graph A and the subsurface (partially saturated to fully saturated soil) is shown in Graph B. The NRCS for the subsurface interface is typically on the order of or greater than the surface due to the wavelength in the material.

becomes small with respect to the radar's wavelength, the gradient can be approximated as a step change in saturation.) Figure 6 shows the NRCS of the surface and subsurface for various saturation fractions of the partially saturated vadoze zone (see Fig. 3). The subsurface exhibits a larger cross-section due primarily to the change in the wavelength (which has a λ^2 effect on the RCS).

In Fig. 6, a subtle variation in the NRCS as a function of frequency is observed as a deviation from the nearly linear trend. The characteristic impedance of the material (and its propagation velocity) are dependent on the variation in permittivity and conductivity. As the conductivity of the material changes, it has a nonlinear effect on the NRCS which is illustrated in Fig. 7. To evaluate the effect of the material's conductivity on the surface's NRCS (using Eqn. 27), the permittivity of the partially saturated soil (with $S_w = 0.1$) is taken from the model presented in Fig. 5 and the conductivity is varied according to the graph's x-axis to show the NRCS's dependence on both frequency and conductivity.

To this point, we have considered the effects of loss in material due to absorption of the energy primarily through conduction losses. In reality, the extinction (i.e., attenuation or loss) of the forward-propagating field within a volume is due to both absorption and scattering of the energy. Similar to the RCS in Eqn. 19, these are represented by the extinction, total scattering, and absorption cross-sections $\sigma_{ext} = \sigma_s + \sigma_a$.
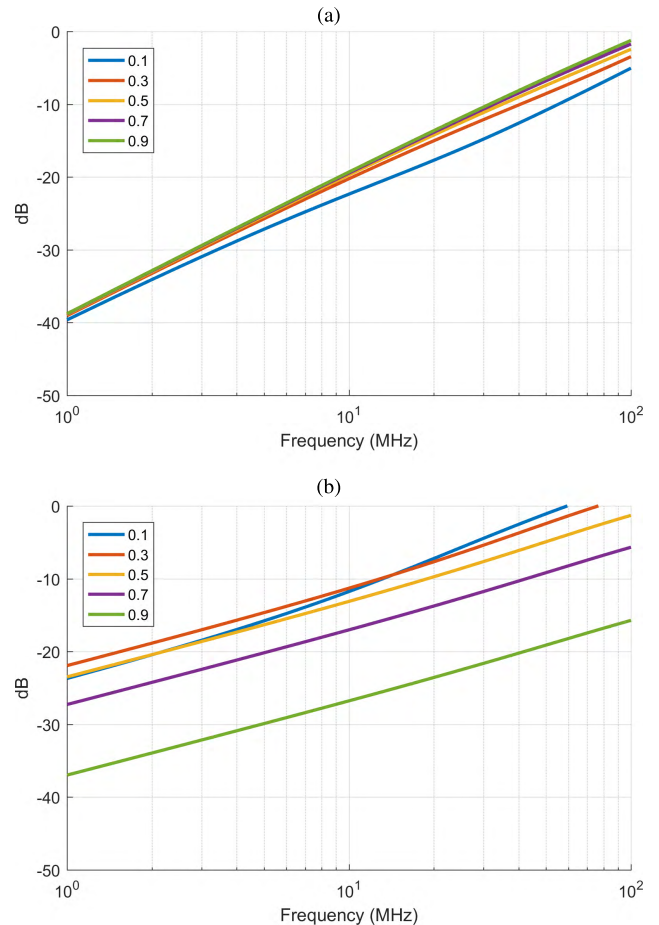
The previous discussion on attenuation assumes that all extinction is due to absorption in the form of conduction loss. The scattering losses, σ_s, represent incident power that is scattered. The scattering losses are a function of the electrical size and physical structure of the medium. For physical structures where lengths become large with respect to the wavelength (typically when $l > \lambda/10$), the scattering losses can exceed absorption losses. If these structures and particles are small with respect to the wavelength (i.e., in the Rayleigh scattering regime), then absorption losses dominate. As the dimensions of the subsurface structures become large with respect to the wavelength in the subsurface (approximately $l > \lambda/10$), the effects of Mie or optical scattering becomes non-negligible and the scattering losses can be on the order of or significantly higher than absorption losses.

The scattering losses are the result of incident power being scattered in directions other than the direction of propagation. This scattered energy is redirected to propagate in other directions. Some of the redirected power will ultimately
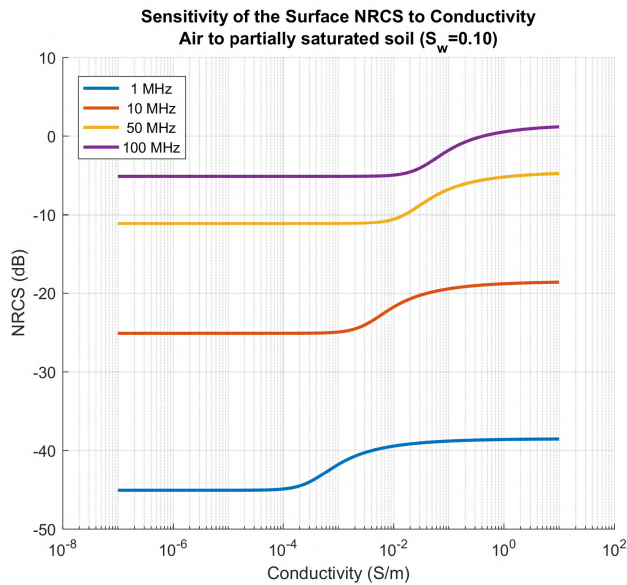
IEEE Access

R. M. Beauchamp *et al.*: Can Airborne GPRs Explore Groundwater in Hyper-Arid Regions?

FIGURE 7. The effect of changes in material conductivity and frequency are observed in the two-layer model's estimated NRCS for the air to partially saturated soil interface ($S_w = 0.1$).

scatter a second time with some portion eventually returning to the radar. This energy will be received and constitutes a portion of the received signal that is due to "multi-path" reflections. This bistatic scattering can be polarimetrically diverse and can be sensitive to changes in observation geometry. Using polarimetry and spatial diversity, these multi-path echoes may be more easily distinguished (albeit, potentially at significantly reduced power) from the monostatic radar signature.

A number of field studies consider the impact of scattering losses on the overall signal attenuation. Observations in Volcanic Tableland near Bishop, CA [27] compare estimates of loss using GPR with resistivity measurements. The GPR results exhibit an excess loss as compared to the absorption losses estimated from the resistivity measurements. The excess loss is attributed to scattering loss caused by the heterogenous subsurface with structures on the order of a wavelength. As the GPR's frequency increases, the excess loss is observed to increase indicating an increase in scattering loss. From a separate study of large sand dunes in the Amargosa Desert, Nevada [28], Heggy *et al.* conclude that the scattering losses are negligible given "few internal structures" of the homogeneous eolian sand. Numerous sand dunes were observed in the United Arab Emirates using a GPR centered at 28 MHz [29] and the results show a wide variation in subsurface penetration depths even within relatively small horizontal changes. This is likely due to variations in material properties but is also a function of structure and scattering losses. At high frequencies, near surface results (e.g., attenuation, loss, material composition) cannot be extrapolated to deeper depths due to variability in structure and materials which cannot be assumed as homogeneous in depth.

From these example studies, the significance of scattering losses are determined on a case-by-case basis but general characteristic behaviors can be summarized. In general, longer wavelengths are less susceptible to scattering loss (and from our earlier discussion, exhibit lower absorption losses). The homogeneity of the subsurface determines the loss due to scattering. Nominally, a homogeneous subsurface will have no scattering losses while a rough or layered heterogeneous subsurface will exhibit higher (and potentially significant) losses from scattering. Because the losses are dependent on the spatial (vertical) variation of the material, the characteristics near the surface cannot reliably be extrapolated to deeper depths (the material composition becomes uncorrelated as depth increases). As one might expect, as the absorption loss decreases, the radar performance estimates get more dependent on accurate estimates of scattering losses as they can become a significant fraction of the total extinction cross-section.

B. ELECTROMAGNETIC PROPERTIES OF MATERIALS

The dielectric relative permittivities of soils are typically around 3 for dry sands and may exceed 30 for saturated sands and silts. This includes the expected range of permittivities for most materials including limestone, sandstone, shale, and clay. The dielectric permittivity of common geologic materials are presented in Table 3 [21]. At lower frequencies (approximately < 10 MHz) there may be an increase in the effective permittivity due to the polarizability of the pore fluid within the soils lattice [23].

TABLE 3. Relative permittivity ranges of common materials [21].

Dry Sand	3 to 5
Saturated Sand	20 to 30
Limestone	4 to 8
Silts	5 to 30
Granite	4 to 6
Ice	3 to 4

Review of Fig. 5 shows a nonlinear response in conductivity and permittivity as a function of saturation fraction. The sensitivity to changes in the bulk material conductivity and permittivity with respect to S_w are typically much higher at low S_w (i.e., near $S_w = 0$) than for high S_w (i.e., near $S_w = 1$). The derivative of the conductivity and permittivity with respect to moisture content are observed to decrease and become approximately constant as the saturation increases beyond 10-30% water saturation. This inflection point is material dependent but is shown to be related to the water saturation fraction where the surface area of the soil grains within the volume are fully coated with an aqueous layer [30]. The magnitudes of the changes at low saturation fraction are also determined by residual salts within the grain structure that become hydrated. Table 4 illustrates the ranges of conductivity for various potential pore fluids. The conductivity is largely influenced by dissolved solids in the water; this is apparent when comparing "salt lakes" to "very pure waters".

R. M. Beauchamp *et al.*: Can Airborne GPRs Explore Groundwater in Hyper-Arid Regions?

IEEE *Access*

TABLE 4. Conductivity of water in the region of the Great Lakes [31] as a range of pore fluid conductivities that can saturate soils.

Type	mS/m
Meteoric waters (from precipitation) 1 to 30 Surface waters (lakes & rivers)	0.3 for very pure waters
Surface waters (lakes & rivers)	10,000 for salt lakes
Surface waters in igneous regions	2 to 30
Surface waters in sedimentary regions	10 to 100
Soil waters	average around 10, but up to 10,000
Groundwater in igneous regions	6 to 30
Groundwater in sedimentary regions	1,000
Mine waters (copper, zinc etc. i.e. sulfates)	not usually less than 3,000

The bulk conductivity of the soil typically exhibit a strong dependence on the salinity of the pore fluid.

Knight and Abad [32] considered the rock-water interaction by comparing the measured permittivity in both untreated sandstone and sandstone which was treated with a hydrophobic coating. The sandstone that was treated with the hydrophobic coating are in good agreement with models that are simply a linear combination of the material properties for the appropriate volume fractions of water, air, and dry sandstone. This is to say that the derivative of the conductivity and permittivity of the hydrophobic sandstones are shown to be approximately constant for all saturation factions. For the untreated sandstone, the linear combination can be used, but is typically only valid for above the critical saturation point with an artificial intercept value of σ_s and ϵ_r at $S_w = 0$. (The intercept is artificial because it may not be representative of any of the constituent material's properties and is only applicable for a range of S_w.)

For the range of expected subsurface conductivities (approximately 0.001 S/m to >1 S/m) and the frequencies we are considering, the high-freqeuncy relaxation response of the material can be ignored and the DC conductivity dominates (i.e., $\sigma_c \gg \omega\epsilon''$) [28], [33], [34]. This allows the use of DC and low frequency conductivity measurements to estimate the dielectric loss for the range of frequencies being considered. Note that resistivities are commonly reported for geological surveys. Resistivity, measured in Ohm-meters (Ohm-m or Ω-m), is the inverse of conductivity, measured in Siemens per meter (S/m).

The expected range of conductivities is between 0.0001 S/m for dry unconsolidated gravel to > 1 S/m for brine-saturated sand and gravel. Dry sand with low salt content is expected to have conductivities on the order of 0.0001 and 0.001 S/m. The IEEE guide for Earth Resistivity [35] classifies resistivities; 10000 Ohm-m (0.0001 S/m) is an "unusually high" resistivity and 10 Ohm-m (0.1 S/m) is "unusually low". From inspection of these classifications, nominally the conductivities may be approximated as a log-Normal statistical distribution. It Is worth noting that the resistivity can vary orders of magnitudes with changes in salinity, moisture, and temperature. A review of resistivities (and conductivities) reports typical resistivities between 20 Ohm-m and 200 Ohm-m for realistic geological conditions (i.e., not laboratory settings with ideal materials). Although less frequent, examples with measured

resistivities > 1000 Ohm-m are reported, but these generally correlate to dry unconsolidated materials (e.g., gravel or coarse sand). Refer to Table 5 for an example of typical ranges for common soil and subsurface materials. Again, note that these resistivities are sensitive to local conditions and may vary significantly with changes in soil structure and pore water salinity.

TABLE 5. Approximate resistivity ranges of some soil materials (adapted from Table 1 of [36]).

Materials	Resistivity (Ohm-m)
Ashes	3.5
Clay soil — 40% moisture	7.7
Clay soil — 20% moisture	33
Clay — London	4-20
Clay — very dry	50-150
Chalk	50-150
Coke	0.2-8
Consolidated sedimentary rocks	10-500
Garden earth — 50% moisture	14
Garden earth — 20% moisture	48
Gravel — well graded	900-1000
Gravel — poorly graded	1000-2500
Gravel clay mixture	50-400
Peat	45-200
Sand — 90% moisture	130
Sand — normal moisture	300-800
Sand clay mixture	200-400
Surface limestone	100-10,000

Material properties are significantly influenced by moisture and temperature [36]. Figure 8A illustrates the impact of moisture content on the resistivity of three soil types. A review of the changes in resistivity with moisture content concludes that the effect of pore fluid on the bulk conductivity can be significant even for partially saturated material. Similarly, Fig. 8B demonstrates the effect of temperature on soil conductivity. For frozen water (ice), the resistivity can be an order of magnitude higher than for the liquid phase.

While the permittivity plays a role in the specific signal attenuation due to absorption, the range of expected permittivities is expected to generally be in the range of 3 to 30 for the subsurface [21]. The range of conductivities is expected to be between 10^{-4} and 1 S/m [35], [36]. Permittivities and conductivities outside of these ranges exist, but they are expected to be observed infrequently. Figure 9 illustrates the specific attenuation due to absorption at 1 MHz and 10 MHz and highlights typical ranges of relevant materials' properties.
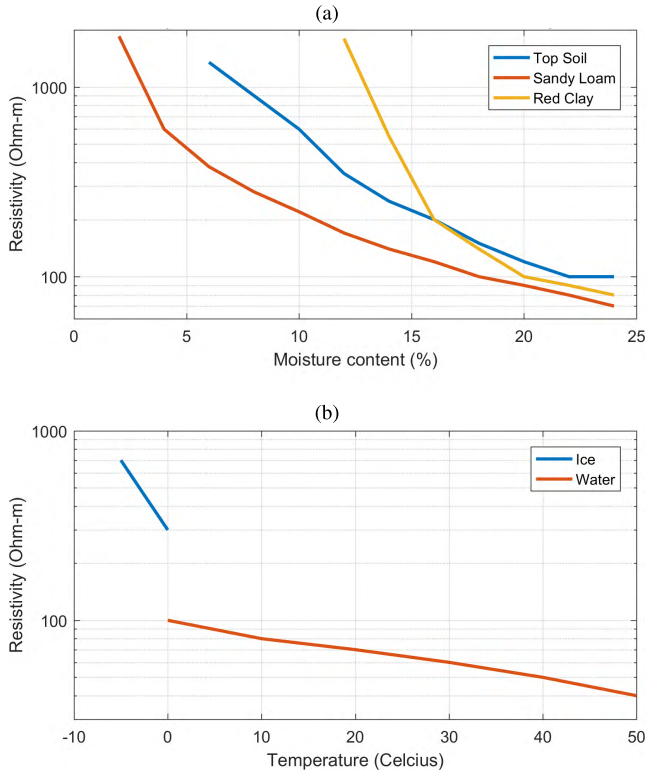
IEEE *Access*

R. M. Beauchamp *et al.*: Can Airborne GPRs Explore Groundwater in Hyper-Arid Regions?

FIGURE 8. The results here are adapted from [36]. Graph A shows the effects of moisture content variation on the bulk soil resistivity for a few different soil types. Similarly, Graph B provides insight into the effects of the pore fluids state and temperature on the bulk resistivity.

IV. SURFACE CLUTTER

In radar applications, "clutter" is a term used to describe unwanted echoes. In particular for subsurface sounding applications (e.g., ground penetrating radar), echoes from the surface are a main source of clutter. This clutter, when its power is higher than that of the signal of interest (e.g., a subsurface feature), can obscure or mask the desired target's features. The clutter, in effect, prevents the radar from detecting the subsurface targets of interest. Any energy received from directions other than those perpendicular to the plane of the surface (the shortest path to the subsurface targets of interest) increases the probability of clutter contamination. To limit the chance of receiving echoes that are not perpendicular to the surface, clutter can be managed by using an antenna that focuses its transmitted power into the ground and that only receives echoes from directions of interest. The antenna's radiation pattern determines the directions the radar is sensitive to when receiving echoes (and the directions it transmits power that can result in echoes). For surface-based GPR, shielded antennas that are as close to the ground as possible are desired to reduce the effects of clutter. As the beam width of the antenna's radiation pattern increases, the surface area illuminated by the antenna increases, which results in increased clutter. Figure 10 shows a conceptual diagram of how changes in the antenna's height impact the signal and clutter power.
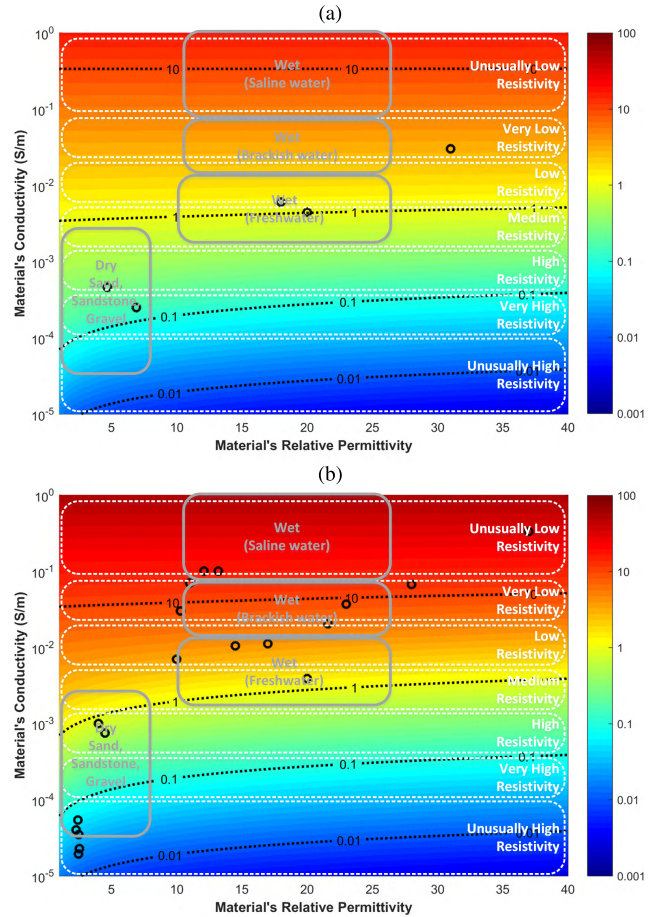

FIGURE 9. The one-way specific attenuation due to absorption is presented at two different frequencies, (a) 1 MHz and (b) 10 MHz, over the range of expected materials' electrical properties. The black dashed contour lines are provided as reference points. The material resistivity classifications (recall resistivity is the inverse of conductivity) are shown as white dashed boxes [35]. The gray solid boxes highlight typical ranges of the electrical properties for soils for dry conditions or wetted with pore fluids of varying salinity. The black circles represent a sampling of measured permitivities and conductivities of various soils and saturations at the indicated frequency. (See [26], [37], [38] for 1 MHz and [26], [38], [39] for 10 MHz).

Next, we analyze the clutter characteristics through a discussion of the surface scattering behavior and of how echoes from large areas (such as the surface) are added at the receiving antenna of the radar. The RCS of a complex-geometry object can be calculated by subdividing the object into a collection of smaller simple objects with known RCSs. The coherent integration (i.e., accounting for phase and amplitude) of the contributions from all simple objects can be leveraged to calculate the RCS of the complex-geometry object. This approach assumes no interaction between components [40].

The same approach can be applied to estimate a surface's RCS. The surface can be divided into patches (or facet), each with its own range (i.e., phase) and RCS. For simplification, we assume that each patch has the same RCS σ_0. First, we consider a coherent surface with each patch at the same range. With N facets, the total observed

R. M. Beauchamp *et al.*: Can Airborne GPRs Explore Groundwater in Hyper-Arid Regions?
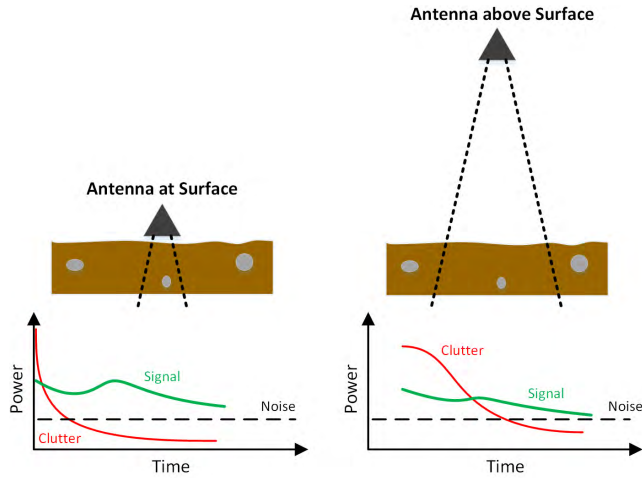
IEEE *Access*

FIGURE 10. A conceptual diagram illustrating the effects of antenna height on the surface clutter response. When the antenna is at the surface, the clutter has a negligible component and signal detection is noise limited. As the antenna height increases, the duration of significant clutter power increases. For this scenario, detecting a signal is typically clutter limited. The depths at which the signal is clutter- or noise-limited are determined by the antenna pattern and height.

RCS can be estimated as

$$\sigma_{coh} = \left(\sum_n^N \sqrt{\sigma_0} e^{-j2\beta r_n} \right) \left(\sum_n^N \sqrt{\sigma_0} e^{-j2\beta r_n} \right)^* \quad (32a)$$

$$= \left| \sum_n^N \sqrt{\sigma_0} e^{-j2\beta r} \right|^2 = N^2 \sigma_0. \quad (32b)$$

Then, we consider an incoherent surface whose facets are uncorrelated in range with a variance $\sigma_r^2 \gg \lambda$ and an integration range larger than a wavelength $\Delta R \gg \lambda$. Under these assumptions, the resulting surface RCS is

$$\sigma_{incoh} = \left(\sum_n^N \sqrt{\sigma_0} e^{-j2\beta r_n} \right) \left(\sum_n^N \sqrt{\sigma_0} e^{-j2\beta r_n} \right)^* \quad (33a)$$

$$= N\sigma_0 \quad (33b)$$

where $*$ denotes a complex conjugation. Notice that the coherent surface has an area-squared (i.e., N^2 for this example) dependency while the incoherent surface only has an area (i.e., N) dependency. The correlation of the surface height over the area determines the degree to which the surface is coherent vs. incoherent for the given wavelength (i.e., its roughness). These coherency scales are wavelength dependent, so in general, longer wavelengths will tend to be coherent for a given surface roughness while shorter wavelengths will tend to see an incoherent surface. Note that in these equations, N is proportional to the surface area A_s.

The projection angle of the plane wave onto the patch also determines the illuminated area (i.e., the patch's area projected onto the plane wave) [41]. As such, when the incident angle is varied (the incident and scattering angles are the same for a monostatic radar system), the magnitude of the apparent

RCS varies according to

$$\tilde{\sigma}_0 = \sigma_0 cos^2(\theta_i). \quad (34)$$

The polarization dependence is not explicitly accounted for (and therefore may have a second-order effect). The incidence angle only represents the change in the geometric projection of the incident power and treats the patch as a "point" scatterer.

With a model for the NRCS of the surface, the radar's observed surface RCS is the integration over the entire surface area illuminated by the transmitted signal. The surface area illuminated by the radar pulse is a function of the transmitted pulse width and the antenna pattern (we assume a monostatic system here). The transmitted pulse width occupies an equivalent range (recall the range resolution of the pulse) which, when projected onto the surface, determines the illuminated area of the pulse. The antenna pattern, when projected onto the surface, also illuminates a finite area. If the pulse's area is greater than the antenna's illuminated area, the radar is said to be "beam-limited". Alternatively, if the pulse's area is less than the antenna's area, the radar is said to be "pulse-limited". Figure 11 illustrates the pulse's projection onto a flat surface and the surface area that is illuminated but the radar. For the pulse-limited case, the leading and trailing edge of the transmitted pulse can be on the surface illuminating an area while still in the antenna's main lobe. In either case, the effects of the pulse, antenna, and surface geometry must be accounted for to accurately assess the radar response of the surface [42]. It is also worth noting that the pulse-limited power decays as R^3 while the beam-limited power decays as R^2. (Compare this to the R^4 power dependence for a point scatterer.)

The beam-limited area of the circle illuminated on a flat surface, for a radar at height h above the surface with a range R to the leading edge of the pulse, is

$$A_s = \pi \left(R^2 - h^2 \right). \quad (35)$$

Similarly, the pulse-limited area is estimated following

$$A_s = \pi(R_2^2 - R_1^2); \quad R_1 \geq h, \; R_2 \geq R_1 \quad (36)$$

where R_2 and R_1 are the leading and trailing ranges of the pulse. The leading and trailing pulse edges are separated by the range resolution of the transmitted signal $\Delta R = R_2 - R_1$.

A. SIMULATED SURFACE CLUTTER RESPONSE
Surface roughness is typically treated in a statistical sense. The exponential correlation model is a common model to characterize the surface roughness [43]–[45]. Arid regions and alluvial fans typically exhibit surface features that are approximately smooth to the radar frequencies of interest [44]. Recall that when a surface is "smooth" at a given frequency (i.e., the P-band results from [44]), it remains a smooth surface at lower frequencies. For areas with minimal vegetation, the surface morphology dominates when determining the radar signal's coherence as the surface itself is
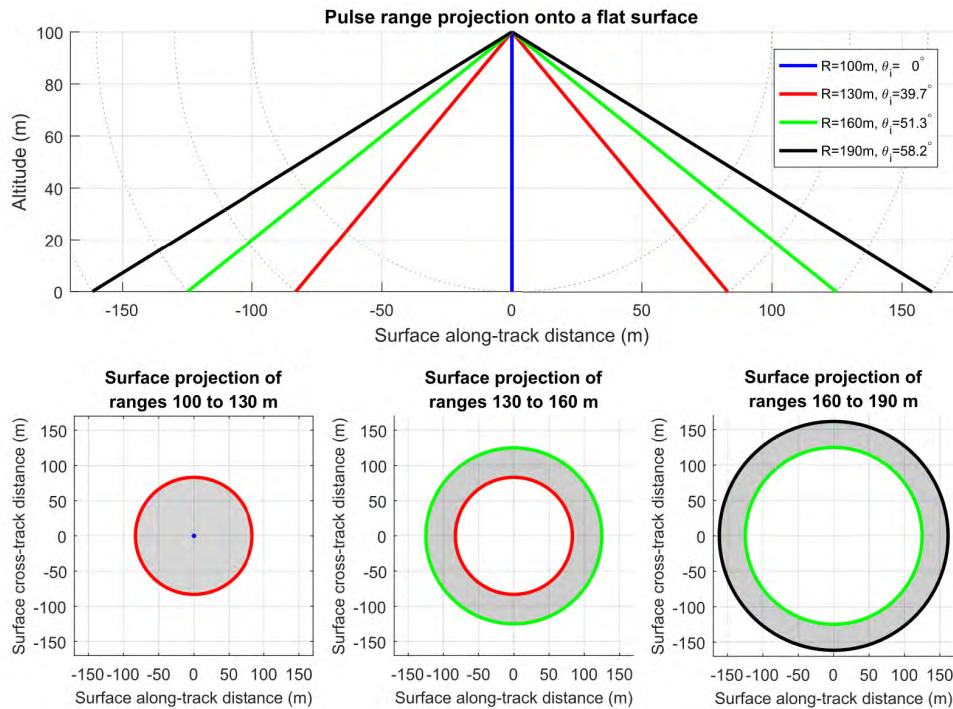
IEEE *Access*

R. M. Beauchamp *et al.*: Can Airborne GPRs Explore Groundwater in Hyper-Arid Regions?

FIGURE 11. The pulse's range from the radar, in addition to the pulse's range resolution and the radar's operating altitude, determine the pulse's projection onto the surface that will produce the received echo. The surface areas which are illuminated for various ranges are illustrated for a flat surface. For this example an altitude of 100 m and a range resolution of $\Delta R = 30$ m is shown. The surface's angle from nadir (θ_i) are included for the highlighted ranges.

the dominant scatterer. This indicates that topographic maps should provide realistic estimates of the clutter response for arid regions at low GPR frequencies.

To simulate the surface clutter for a specific region, a model of the surface topography with sufficient resolution is required to capture the variation (which is wavelength and surface roughness dependent). Again, when using a coherent scattering model, the surface should be resolved to a fraction of a wavelength (ideally 0.2λ to 0.1λ). Alternatively, a statistical roughness model can be used; it accounts for the coherency of the surface features and the power from each surface element (which has lengths $\gg \lambda$) can have their power summed (i.e., incoherent summation).

For this application, the wavelengths of primary interest ranges from 300 m (1 MHz) to 3 m (100 MHz). A digital elevation model (DEM) from the shuttle radar topographic mission (SRTM) is available at a 1 arc-second posting (approximately 30 m spatial resolution) and with a surface height resolution of 1 m. To apply this DEM to the wavelengths of interest, the 30 meter resolution data is interpolated to sub-wavelength scales to use the coherent scattering model without additional modeling of the patches' RCS. The height and orientation of each patch are calculated from the DEM to be subsequently used in the estimation of clutter power. Figure 12 is an example of the DEM for a region in Saudi Arabia.
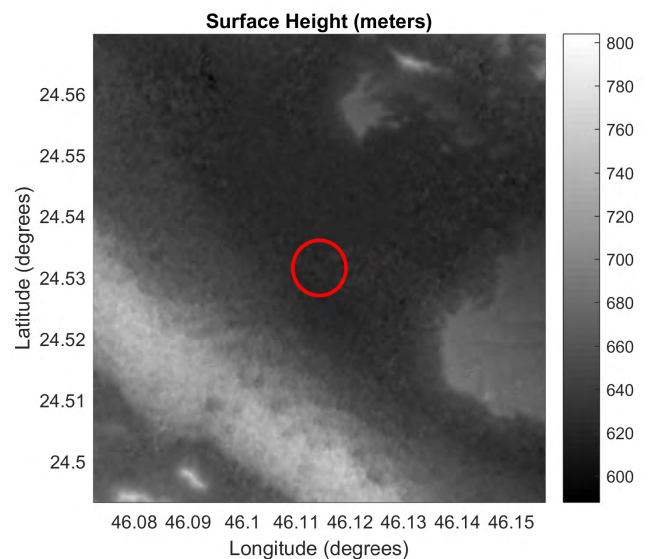

FIGURE 12. The SRTM digital elevation map for an experiment site in Saudi Arabia. The red circle is 1000 meters in diameter, providing a scale for reference. This site is used to simulate and analyze the expected clutter signature.

To simulate surface clutter, the transmitter and receiver are modeled as isotropic point sources at a fixed altitude. The SRTM DEM is interpolated (using a spline) to 1 m resolution for the region in Fig. 12. The NRCS of each patch is 0 dB with an angular dependence following Eqn. 34. For the results
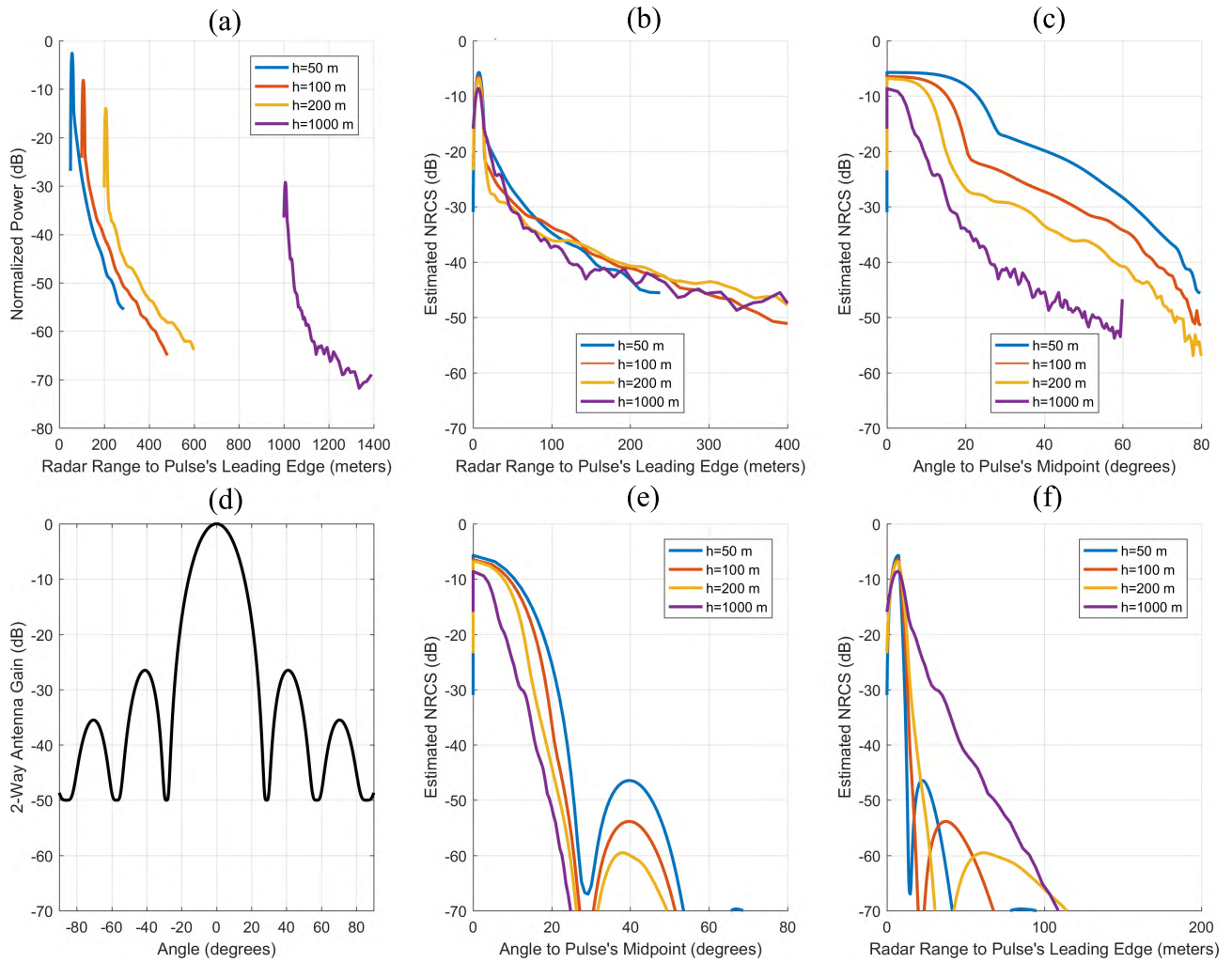
R. M. Beauchamp *et al.*: Can Airborne GPRs Explore Groundwater in Hyper-Arid Regions?

IEEE*Access*

FIGURE 13. The received range response of the clutter echo's power is simulated at four different radar heights with an isotropic antenna (a). In (b), the NRCS is calculated and plotted versus the range in excess of the height (i.e., the radar's height is subtracted from the true range). Using the NRCS from (b), the range is converted to incidence angle in (c). The estimated NRCS is estimated for the directional antenna pattern of (d) and presented as a function of surface incident angle (e) and range in addition to the radar's height (f).

presented in Fig. 13, the range resolution of the simulation was set to 15 m and the arithmetic mean was calculated using 30 realizations of randomly positioned "radars" at a constant altitude above the point directly below the radar. The surface clutter's normalized received power (P_r/P_t) from the simulation is presented as a function of range from the radar in Fig. 13A. P_r and P_t are the received and transmitted power of the simulated radar. For the graphs which are presenting the simulated NRCS, it is estimated by $\widehat{\sigma_0} = \widehat{\sigma}/A_s^2$ where $\widehat{\sigma} \approx P_r R^4/P_t$. Again, the antenna model used to produce the results in Fig. 13A-13C is an isotropic (unity gain) antenna on both receive and transmit. The simulated radar heights are 50, 100, 200, and 1000 meters above the surface point at nadir.

Figure 13B shows the clutter response for different altitudes as a function of the range in excess of the radar's nadir distance to the surface. The same clutter response is also presented as a function of pulse's incident angle (Fig. 13C). In Fig. 13B, a 0 m range to the pulse's leading edge of the

transmitted pulse indicates the first instance of a returned echo. With a range resolution of 15 meters, when the range to the pulse's leading edge is 15 m or larger, the entire pulse is contributing to the echoes which are coherently integrated over the illuminated surface area. When the range to the leading edge is equal to the pulse's range resolution (nominally its width), this is statistically the range at which the peak echo power is observed. When the entire pulse is illuminating the ground, all of the power is available to be reflected and, at the instant when all power has reached the surface, it has the minimum area and statistically, the highest coherence. As the area increases, the coherence decreases (and the incident angle also increases which, following Eqn. 34, reduces the effective NRCS).

If the surface was perfectly coherent over the illuminated area, without any incident angle dependence, the estimated NRCS from our simulation in Figs. 13B-13C would be 0 dB for all ranges/angles. (Note that 0 dB is the NRCS of the

IEEE Access

R. M. Beauchamp *et al.*: Can Airborne GPRs Explore Groundwater in Hyper-Arid Regions?

patch used for the simulation.) If the wavelength is increased, the area's coherence is also increased. Note that the range resolution (ΔR) defines the integration length which acts as a convolution window. As the range resolution becomes larger, the coherent peak is extended in range (or incidence angle). The roll-off rate (the change in the estimated RCS with respect to range) would remain the same but would be observed at an increased range. Consider the consequences of the effects on this clutter signature due to changes in the wavelength and range resolution. For all pulses, there is an initial coherent surface response and longer wavelengths increase the coherent area. At our wavelengths of interest, the range resolution of the signal primarily determines the extent in "range" at which the coherent impulse is observed due to the convolution effect. The rate at which the surface echo decays with range (again, assuming an isotropic antenna) is a function of range-fading for ground-based and low-altitude airborne systems (represented in the R^4 factor that was corrected for to get $\widehat{\sigma_0}$) and the coherence of the wavelength. To maximize the detection probability of subsurface targets near the surface (i.e., $R \approx h$), ΔR should be minimized when the peak clutter echo power is greater than the subsurface echo power. (As a second order effect, the radar frequency should be maximized.) For targets that are located deeper within the medium and further from the surface, the effects of clutter can be reduced by minimizing h or minimizing the antenna beam width.

In Fig. 13B, the clutter response (shown as range beyond the nadir surface distance) is approximately the same for all altitudes. Note that for the 50 m altitude, ranges beyond approximately 240 m were not evaluated in the simulation. In Fig. 13C, the angle to the pulse's midpoint is calculated assuming a flat surface (i.e., surface topography is ignored for calculating the angle). The surface incident angle θ_i is determined by the range to the radar R and the radar altitude h as

$$\theta_i = \cos^{-1} \frac{h}{R}. \tag{37}$$

The estimated NRCS, as a function of incidence angle, for different altitudes is shown in Fig. 13B. Note that the range is the midpoint of the radar signal (i.e., halfway between the leading and trailing edge of the pulse). With a range resolution of $\Delta R = 15$ m, the pulse midpoints at the instance where the pulse is completely on the surface corresponds to angles of 29.6° for an altitude of 50 m, 21.5° for 100 m, 15.5° for 200 m, and 7.0° for 1000 m. These angles represent the inflection point in the estimated NRCS from Fig. 13C where the trailing edge of the pulse starts moving away from nadir creating an illuminated area in the shape of an annulus. The mean distance between points within this area increases with the range to the leading edge and therefore the correlation of surface height decreases. As the altitudes decreases for the same range resolution, the incidence angles between the leading and trailing parts of the pulse increase (following Eqn. 37).

The surface clutter simulations highlight the trade-space that exists between the antenna's beamwidth, the range resolution, the radar's altitude, and the ranges of depths where ground clutter mitigation is most critical. For deep radar sounding applications, the desire is to achieve detection at the maximum possible depth below the surface while meeting the required range resolution. The nadir path is the minimum distance to that depth and therefore, any signals propagating at other angles are not strictly necessary (or in fact, are frequently undesirable). The clutter echo power from off-nadir angles is observed in addition to the nadir subsurface signal. The ratio of signal-to-clutter power (or SCR) is used as a metric to judge the detection probability of a subsurface target. For the purpose of our discussion, the signal power must be greater than the clutter power (i.e., SCR > 0 dB) and the higher the SCR, the better. Given this, it is clear that if the signal from non-zero angles can be reduced, the SCR will be increased.

To increase the SCR for nadir-looking (i.e., $|\theta_i| = 0$) radar sounders, the off-nadir clutter contributions (i.e., from angles $|\theta_i| > 0$) must be suppressed. To illustrate this effect, an example of a notional two-way antenna pattern (the combined effects of the antenna on transmit and receive) is shown in Fig. 13D. This antenna pattern is applied to the surface response of Fig. 13C to give Fig. 13E. Similarly, as a function of range past the nadir surface interface, the effect of the radar altitude and the antenna pattern is clearly observed in the range response of the clutter from Fig. 13F.

The antenna provides directivity to reduce the magnitude of the off-nadir clutter. We can quickly see from Fig. 13F that to effectively attenuate surface clutter, the required antenna beamwidth becomes narrower as the altitude of the sensor increases. The angles for which clutter is a concern depends on range resolution, altitude, and the maximum desired penetration depth. Note, that the actual subsurface range depends on the material properties given the change in propagation speed following Eqn. 13. At lower altitudes, the requirements on the antenna beam width are relaxed for the same desired antenna side-lobe suppression at a given subsurface depth.

V. FIELD EXPERIMENTS

Radio attenuation in sub-surface sounding radar applications, which includes both absorption and scattering losses, where discussed in Section III. The frequency dependency in the 1-100 MHz regime is largely environment and medium dependent; it can be constrained with soil/sand type assumptions for arid desert areas. The soil's conductivity dominates the absorption loss as $\sigma \gg \omega\epsilon$ at lower-frequencies. As the radar's frequency decreases, the trend is that absorption losses will dominate while scattering losses can largely be neglected. In this case, available resistivity measurements in Saudi Arabia can be used to study the radar attenuation at low-frequencies and to constrain the penetration depth. While such a behavior is expected at very low-frequencies, there is little or no experimental evidence from desert environments in Saudi Arabia to confirm this theory and to constrain the

R. M. Beauchamp *et al.*: Can Airborne GPRs Explore Groundwater in Hyper-Arid Regions?

IEEE *Access*

range of frequencies where this simplification can be applied. Therefore, a goal of the field experiments was to provide an experimental basis to constrain or define the attenuation models in the arid desert regions of Saudi Arabia.

The field experiments collected very low-frequency electrical resistivity technique (<10 kHz resistivity via a Wenner array). The site selected for the experiments was the Almuzahimiyah site, which is approximately 60 km outside of Riyadh (Fig. 14) at 24.5315° N and 46.1143° E. The surface height DEM in Fig. 12 and surface clutter analysis was evaluated for the area around the experiment site. The relatively flat terrain of the site indicates it's a suitable location for future aerial/airborne testing for cross-validation with ground observations. The resistivity measurements were collected on two lines shown in Fig. 14. Due to the collection of field data during the wet/rainy season in April 2017, resistivity data collected during two previous dry seasons in 2015 and 2016 in a nearby site were added to complement the analysis. The resistivity measurements were collected over a distance of about 700-900 m. The two-dimensional images of resistivity (along-track distance versus depth) were estimated from the measurements using the RES2DINV software [46].
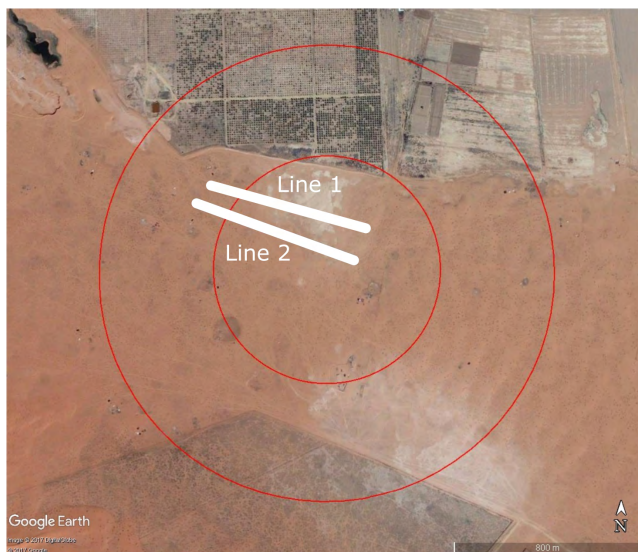

FIGURE 14. The study area located about 60 km outside of Riyadh, where resistivity measurements were collected along two parallel lines. The concentric red circles are 1 and 2 km diameter for scale.

The resistivity results in Fig. 15 from the wet seasons show similar trends for both lines, and resistivity results from the dry seasons in 2015 and 2016 also show similar trends, suggesting that the data collection and inversion techniques for 2D resistivity maps are repeatable. Cumulative distributions of the resistivity data for multiple ranges of depths are shown in Fig. 16. From these CDFs, it can be seen that the resistivity values in the same location can be about an order of magnitude or more different between the dry and wet season. Considering all depths obtained from the 2D inversions, at least 80% of resistivity values are below about 40 Ohm-m during the wet seasons, and more than 80%
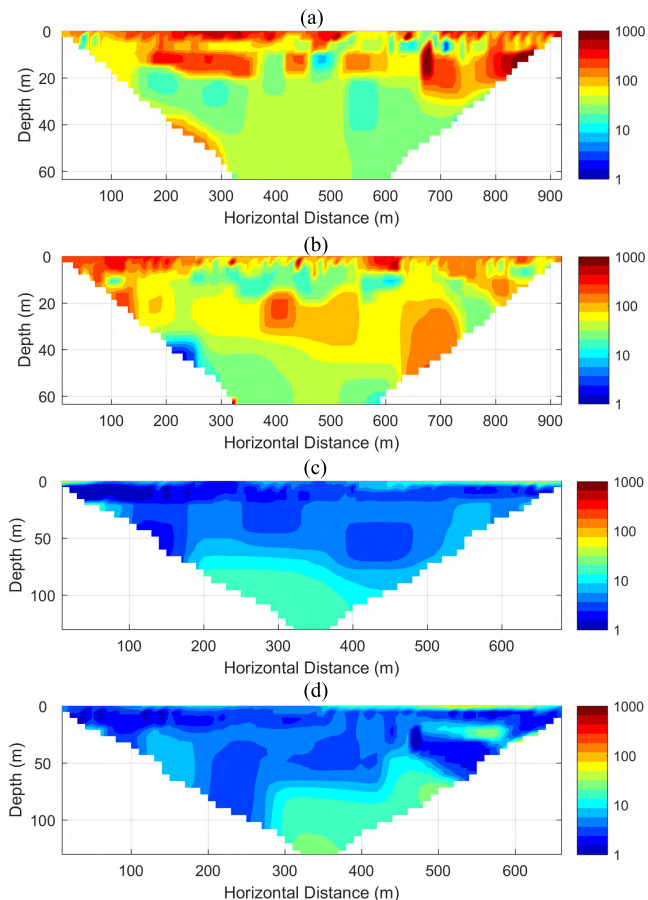

FIGURE 15. Electrical resistivity measurements during the dry and wet seasons show significant differences attributed to the water saturation and content in the ground. Repeat measurements at different times or lines show good repeatability. All resistivity measurements are in Ohm-meters: (a) 2015 Dry Resistivity, (b) 2016 Dry Resistivity, (c) Line 1, 2017 Wet Resistivity, and (d) Line 2, 2017 Wet Resistivity.

of resistivity values are below about 400 Ohm-m during the dry seasons. Comparison of the CDFs of resistivities near the surface typically show higher resistivities than those at deeper depths which are indicative of drier conditions near the surface. From the wet season data, the CDFs indicate much lower resistivities for depths below 10 m. Comparing the dry season surface data (0 m to 5 m depths) to the CDFs from 10-20 meters below the surface (and even the 25 m to 50 m depths for the 2015 data), the CDFs all exhibit similar resistivity values which indicate similar moisture distributions for these depths in dry season conditions.

Comparing our results to publicly available resistivity datasets from the region [47], we find the resistivity values measured at the Almuzahimiyah site during the dry seasons to agree well with the published data of resistivity from the sandy soil areas near Riyadh (with a minimum of 70 Ohm-m, an average of 131 Ohm-m, and a maximum of 275 Ohm-m). Again, the resistivity observations at the Almuzahimiyah site during the wet seasons are approximately an order of magnitude lower than the dry season results due to the increased soil water content. Figure 17 shows a comparison between measured electrical resistivity
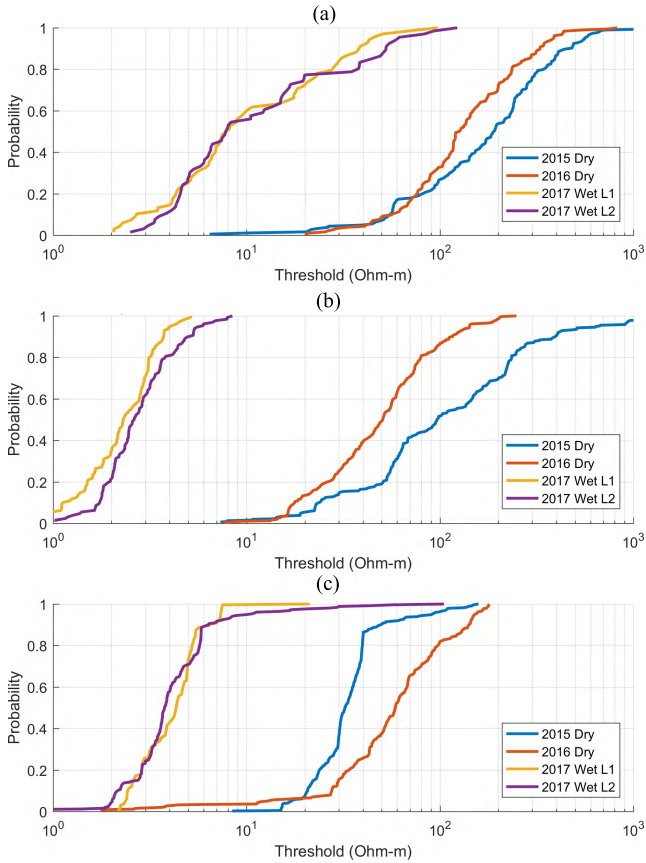
IEEE *Access*

R. M. Beauchamp *et al.*: Can Airborne GPRs Explore Groundwater in Hyper-Arid Regions?

FIGURE 16. The graphs shows the cumulative probability that the observed resistivity values are below a given threshold. Graphs (a), (b), and (c) cover different depth intervals below the surface: (a) 0 to 5 m, (b) 10 to 20 m, and (c) 25 to 50 m. These statistics show good repeatability between measurements in both the dry season and the wet season. An order of magnitude difference between observations in the wet and dry seasons is also observed.

data from the same region. Resistivity data collected during the dry seasons are found to be repeatable (2015 and 2016) and relate well to published resistivity data collected from nearby areas with sandy soils [47].

VI. AIRBORNE RADAR SYSTEM CONCEPTS

A "wide bandwidth" radar system is necessary to achieve range resolutions of tens of meters at sufficiently low radar frequencies to enable deep subsurface sounding. For wideband designs (approximated as $B > f/10$), frequency dispersion is a challenge. While high resolution may be possible near the surface, the higher frequency components will attenuate below the noise threshold as the depth increases and only lower frequencies are available (resulting in a reduced signal bandwidth). Frequency dispersion and frequency dependent effects in the system (specifically, the antenna) are more complex for wide bandwidth systems.

Following the trend that lower frequencies experience less attenuation, it is desirable for a subsurface sounding radar system to operate at the lowest freqency possible, but the side effect is that the wavelengths become substantially large. As antenna size scales with wavelength, high frequency (3-30 MHz) antennas are on the order of 50 m to 5 m. These
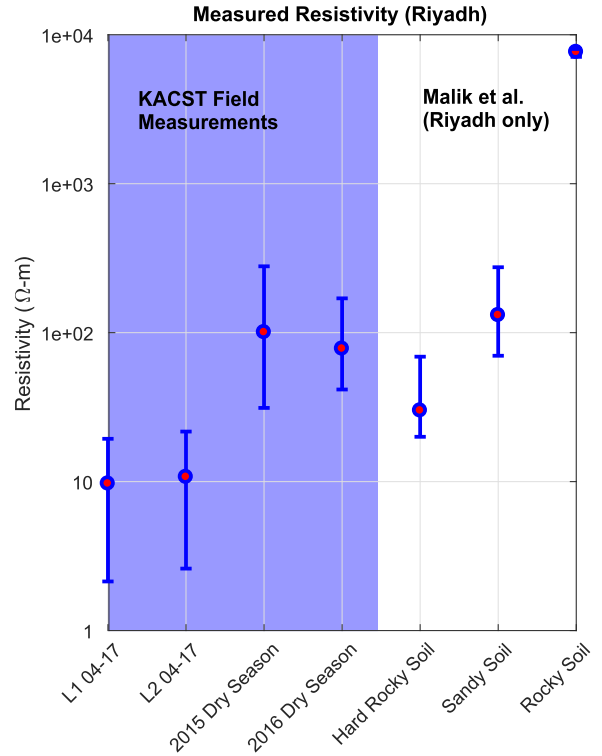

FIGURE 17. Comparison between resistivity field data and publicly available resistivity data sets in the region [47].

antennas sizes can be impractical for an airborne radar system. Electrically small antennas (ESAs) show promise to mitigate the issue of large radiators. ESAs, as defined by the Chu Limit [48], have a high quality factor (high-Q) which leads to a small bandwidth. (Recall that the bandwidth, B, is inversely proportional to range resolution ΔR.) A larger bandwidth is desired to obtain a finer range resolution to differentiate the surface response and resolve subsurface structure. One solution to this problem is to use multiple antennas, each one representing a sub-bandwidth of the total desired frequency range [49]. The concatenated bandwidths of all these antennas would form the desired overall bandwidth. After integrating the radar returns of the sub-bands, radar processing would be done as if a single radiating element was used.

Another method for widening the bandwidth is to resistively load the antenna. Due to the high-Q of ESAs, the antenna will cause excess internal reflections of the traveling wave when sourced with a pulse [50]. Loading the antenna with resistive elements lowers the Q, and thus broadens the bandwidth. This in turn dampens the internal reflections, allowing the initially fed pulse to propagate unperturbed. A side effect of resistive loading is reduced antenna efficiency (i.e., lower antenna gain). Reduced antenna gain can place more stringent requirements on the rest of the radar system's performance to achieve the desired sensitivity.

A. EXAMPLE INSTRUMENTS

From the analysis presented in the previous sections, attenuation and clutter effects were shown to be a limiting factor for

R. M. Beauchamp *et al.*: Can Airborne GPRs Explore Groundwater in Hyper-Arid Regions?

IEEE *Access*

detection of subsurface features. These have been considered for airborne-based subsurface radar sounding applications with a focus on desert environments. The radar frequency ranges under consideration were driven by some measure of prior knowledge about the performance of GPR systems (with regard to clutter and signal attenuation) and airborne ice sounders (with regard to clutter and implementations of airborne radar systems). Examples low-frequency radar systems used to remotely sense the subsurface, whose performance are applicable to airborne subsurface sounding applications, are found in the literature and a few radar examples are detailed in the following paragraphs.

The selection of a radar's operating frequencies is dependent on science requirements and the availability of suitable technology. A general trend in the GPR results and the associated systems' design is to achieve deeper radar sounding depths, hence lower operating frequencies are required at the expense of range resolution. In the next paragraphs, we will discuss systems that have demonstrated radar sounding in ice or desert for the depths of interest from both surface and airborne platforms.

A surface-based, 1-5 MHz GPR [51]–[53] was designed to achieve deep (> 200 m) radar soundings of geological structures. This radar can operate in a monostatic or bistatic configuration with a 35 m long transmitting antenna. From observations in the West Egyptian Desert [53], Ciarletti *et al.* claim to detect the water table interface at 210 m below the surface. These results are contested in [54] on the basis that the region's conductivity leads to negligible ground penetration. The observed echos, which the original analysis attributed to subsurface features, are in fact likely due to ground clutter from local surface features. The interpretation (or misinterpretation) of these results highlights the need to understand the nature of the clutter environment and the impact of subsurface properties on the radar's performance.

The WISE ice sounding radar [55] is an airborne radar operating between 2-5 MHz. This system has been demonstrated in Greenland, Antarctica, and Alaska for subsurface radar imaging in wet ice environments. The system demonstrates the capability to fly and operate a low-frequency, wide-band radar for subsurface sounding. Comparison of the WISE's low-frequency soundings with higher frequency ice radar have demonstrated a reduction in scattering losses due to the lower operating frequencies (in addition to reduced absorption losses due to water). Note that the antenna's physical size (120 m length) and the low gain for the wide-band, low-frequency system present technical challenges.

GPR observations of sand dunes in Nevada for radar frequencies from 16-100 MHz are considered and in part used to investigate subsurface features by comparison with resistivity measurements from other instruments (in particular, TEM soundings) [28]. The electrical properties of samples from the local environment were measured in the laboratory and presented but even the authors note that laboratory measured loss tangents are not representative of the subsurface due to moisture and salinity variations. The paper

reports subsurface resistivity (from TEM measurements) of 6-8 Ohm-m at 35 m depth and 1-2 Ohm-m at 65-75 m depth which is attributed to an increase in pore fluid salinity with depth below the alluvium. The resistivity in the sand dune is 600 Ohm-m and the alluvium's resistivity is approximately 60 Ohm-m. The 100 MHz GPR sounding in this environment was limited to approximately 4-6 m in the alluvium. Even with the 20 MHz sounding, the penetration depth is likely limited to approximately 12 m due to the high loss of the subsurface.

GPR observations of a gravel pit were examined to determine maximum penetration depths for 25, 50, 100, and 200 MHz antennas [56]. Using the 25 MHz antenna, the authors were able to detect features at 52 m (and possibly 57 m) depth. From characterization of 250 different field experiment sites, the authors conclude that the gravel pit site represents the maximum probable GPR depth that can be confidently interpreted from any Quaternary unconsolidated sediments. (Note, the system's SNR and its dynamic range are not reported and the maximum possible penetration depth is a function of the system's technology. This does however highlight the ideal material for deep GPR penetration.) Their results from multiple GPR frequencies show a $\log_2 \lambda$ trend in penetration depth. The reported trend is generally in good agreement with the transition from good conductor to a general dielectric material that is discussed in Fig. 2.

To characterize the subsurface structure of sand dunes in the Mojave desert of California, GPR at 100 MHz and 200 MHz were employed [57]. The results show sounding depths of greater than 30 m for the Dumont dunes and 40 m for the Eureka dunes using the 100 MHz GPR system. These results indicate that sand dunes can be low loss and ideal for GPR investigation. If we assume a $\sqrt{f}$ depth dependence (i.e., the subsurface is a good conductor) and the subsurface remains homogeneous, the expected depth of penetration could be $30\sqrt{100/5} = 134$ m or $40\sqrt{100/5} = 178$ m at 5 MHz, respectively.

In a seperate study, sand dunes in Eastern Saudi Arabia and Moreton Island in Australia were observed using a GPR at 100 MHz, 300 MHz, and 500 MHz [58]. The maximum depth observed was < 35 m at 100 MHz and approximately 9 m at 500 MHz. The authors noted that the water table and saturation gradients within the dune could be detected (when present within the observed depths). Note that the maximum 100 MHz penetration depth of the sand dunes reported here are consistent with the results reported from sand dunes in the Mojave desert of California [57].

Recent advances in GPR technology, in particular signal acquisition and signal preprocessing, are discussed in [59]. The author cites detection of features at depths of 60 m in sand dunes with a GPR operating at 50 MHz and observations to depths > 90 m in sand using a 15 MHz GPR system in Southern Africa. The capability of GPR to image sand dunes in the Sahara desert was evaluated and demonstrated with soundings up to 90 m deep using a 25 MHz system [60]. Depths > 100 m were measured in sand dunes at 10 MHz.

IEEE *Access*

R. M. Beauchamp *et al.*: Can Airborne GPRs Explore Groundwater in Hyper-Arid Regions?

The authors note for the dunes in the Ubari Sand Sea at 10 MHz, that "the instrument produced excellent profiles of dunes to over 190 m penetration". Another experiment provides GPR results for different sand dunes in the United Arab Emirates [29]. For the largest dunes, penetration depths are expected to be greater than 160 m. However, it was also noted that sounding depths could be limited to less than 30 m in some cases. For the measurements, the authors used a radar with a center frequency measured to be 28 MHz in dry sand (the higher dielectric constants load the antenna making it electrically longer, which lowers the antenna's resonant frequency.)

This survey of GPR results and radar sounding instruments demonstrate that low frequency radar sounding (10 MHz or less) can achieve sounding depths of 100 meters or more. This performance is expected for dry, unconsolidated materials with minimal structural variability. Numerous experiments in sand dunes consistently report maximum detection depths when normalized for frequency. This also indicates that scattering losses within the sand dunes have a second order effect on the radar's observed attenuation and absorption dominates for frequencies to 100 MHz or more. GPR operating in the 1-5 MHz band have also been successfully operated for both ground-based and airborne radar sounding operations. At these low frequencies the antenna's physical size presents a challenge to the overall system design and operation.

B. SYSTEM LINK BUDGET

Recall that the radar equation defines the power at the receiver's antenna port as

$$P_s = \frac{\lambda^2 G_r G_t P_t}{(4\pi)^3 R_t^2 R_r^2} \sigma. \tag{38}$$

Using this equation, we can estimate the signal power for a variety of radar system parameters. For our example we consider a monostatic radar system with antenna gains of $G_r = G_t = 0.01$ (-20 dB which is on the order of magnitude for a wide-band resistively loaded dipole) observing at a range of $R_t = R_r = 1000$ m. Our notional radar's transmitted power is $P_t = 1000$ W and operates at a center frequency of 3 MHz ($\lambda = 100$ m). To calculate the received echo power, we consider a pulse-limited transmitted signal with a period of 0.5μS (a bandwidth of 2 MHz and free-space range resolution of $\Delta R = 75$ m). The pulse-limited area is estimated (Eqn. 36) to be 488,910 m^2. If the NRCS is $\sigma^0 = -30$ dB (see Fig. 6), the coherent RCS of the surface is then $\sigma = 26.9$ dB. The received power from the surface echo (at the receiving antenna port) is $P_s = -66.1$ dBm.

We consider the thermal system noise for the purposes of estimating the received noise power. While it is dependent on the system design and operating conditions, we consider two potentially dominant sources of noise. If the antenna's received radiation dominates, we consider

$$P_n^{rec} = G_r k_B T_B B \tag{39}$$

where the Boltzmann constant $k_B = 1.38064852 \cdot 10^{-23}$ m^2 kg s^{-2} K^{-1}, G_r is the receiving antenna's gain, T_B is the effective background radiometric temperature (or brightness temperature) in Kelvin, and B is the bandwidth in Hertz. For this first-order evaluation, we also consider the antenna's noise temperature. The physical temperature of the passive device (in this case the antenna) determines the noise power it generates as

$$P_n^{Temp} = k_B T B. \tag{40}$$

Consider an antenna with $G_r = -20$ dB, $B = 2$ MHz, and $T_B = 300$ K, the received background noise power is then $P_n^{rec} = -130.8$ dBm. For the same antenna, the noise generated due to the antenna's physical temperature ($T = 300$ K) is $P_n^{Temp} = -110.8$ dBm. These simplified models of two potential noise sources provide estimates for an initial evaluation of the notional radar system performance. Here, the power is referenced to the receiving antenna's output port. It should be noted that other components within the radar system may lead to substantially different system noise powers. Other sources of noise (including man-made sources) can also lead to overall higher effective noise powers. Nevertheless, we assume -110.8 dB as the receiver's noise power for comparison.

Comparing the signal power calculated earlier to the antenna's noise power (due to the antenna's temperature), we get an SNR of $P_s - P_n = -66.1 - -110.8 = 44.7$ dB. (The signal in this instance is actually the clutter power.) The noise power remains constant with range.

Next, let's consider a thought experiment: If we have a subsurface interface with the same RCS as the surface, and if the total range between the surface and subsurface target does not change significantly (i.e., $R \approx R_{surf}$), we will have at most 44.7 dB of SNR. Attenuation can only reduce the available SNR. From the examination of the surface clutter as a function of angle, we require the clutter power to drop by more than 44.7 dB from its peak nadir power for the radar system to be consider noise limited. If the clutter power does not drop by more than 44.7 dB for the incident angles of interest (which subsequently correspond to the depths of interest), the radar is considered clutter-limited. The radar is clutter-limited when the SCR is less than the SNR. For clutter-limited cases, there is no advantage in improving the transmitter power or receiver gain (in fact, the TX or RX subsystems may be designed to optimize SCR with respect to SNR). The clutter response can however be altered by modifying the radar's range and the antenna's pattern to reduce the clutter power as shown in Fig. 13.

Clutter is a significant factor that limits subsurface detection in airborne applications (or surface-based radar systems with unshielded, nearly isotropic antennas). The surface response from the nadir direction will always be present (this is the direction we are interested in). After the nadir clutter impulse is passed, the surface response from off-nadir angles are observed. One of the primary means of controlling the clutter is via the antenna pattern and the observation

R. M. Beauchamp *et al.*: Can Airborne GPRs Explore Groundwater in Hyper-Arid Regions?

IEEE*Access*

TABLE 6. Estimated maximum sounding depth for a subsurface target with same RCS as surface clutter. Different signal-to-clutter ratios are considered for different one-way specific attenuation A_1. The corresponding resistivity characterization is from [35] and Fig. 9.

	25 dB SCR	50 dB SCR	100 dB SCR
$A_1 = 0.1$ dB/m (1-10 MHz, dry sand, Very-High/Unusually High Resistivity)	125m	250m	500m
$A_1 = 1$ dB/m (1-10 MHz, freshwater wet sand, Medium Resistivity)	12.5m	25.0m	50.0m
$A_1 = 3$ dB/m (1 MHz, Brackish wet sand, Low Resistivity)	4.16m	8.33m	16.7m
$A_1 = 10$ dB/m (10 MHz, Brackish wet sand, Very Low Resistivity)	1.25m	2.50m	5.0m

geometry. At low radar altitudes, for the same echo range, the incidence angles become larger which allow for relaxed antenna pattern requirements. The clutter's signature also decreases with increasing incidence angle and increasing ratios of the range between the subsurface target and clutter due to range fading (recall that subsurface propagation is slower than free space). Broadly speaking, operating the sounding radar at the lowest altitude possible provides the best performance for deep radar sounding.

Whether the radar is noise- or clutter-limited, subsurface attenuation ultimately limits the detection depths. The specific attenuation that can be tolerated for any given depth is determined by the available SCR (or alternatively the SNR). In Fig. 18, the allowed mean one-way attenuation can be estimated for different SNR/SCR and penetration depths. Assuming that the dynamic range of the radar is with respect to the surface reflection, with SNR/SCR of 25 to 200 dB and a depth of 100 m, 0.1 to 1 dB/m of one-way specific attenuation can be tolerated. (The tolerated loss includes scattering losses.) Assuming 100 dB SCR/SNR, which is representative of a well designed radar system with good clutter rejection, and using Fig. 2 (which assumes $\epsilon_r = 10$ and no scattering losses), the subsurface resistivity at 1 MHz is approximated to be > 500 Ohm-m. Similarly for 10 MHz, the resistivity will likely be required to be > 1000 Ohm-m.
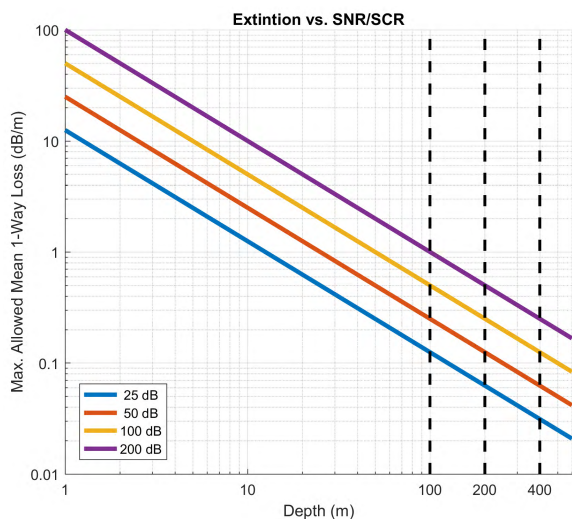
FIGURE 18. Mean specific attenuation allowed for a given signal-to-noise (or signal-to-clutter) ratio at various depths.

To reiterate the theme identified throughout this paper: to achieve deep electromagnetic sounding, lower frequencies are desired. This follows the trends observed in ice sounding

systems as well as commercial GPRs. The literature provides examples of sounding in sand dunes were the authors claim depths of 100-200 m. These are ideal cases in dry sand dunes or unconsolidated gravel and were achieved with ground radar at center frequencies around 10 MHz. The available dynamic range of the radar systems is limited by the ratio of the expected peak echo power (typically the nadir surface echo) to either the noise power or clutter power. Referencing the ranges of attenuation presented in Fig. 9, we consider the maximum depths for a variety of material types and signal-to-clutter ratios in Table 6. A "best case" one-way specific attenuation of $A_1 = 0.1$ dB/m to a very low resistivity material with $A_1 = 10$ dB/m are considered for three different SCR.

The specific attenuation that effects the radar is the total extinction cross-section, combining both scattering loss and absorption loss. Again, recall that as the loss due to absorption decreases, the scattering losses that may have been negligible at higher specific attenuation can be significant when estimating penetration depths. For homogeneous medium, scattering losses can be negligible. For highly variable and heterogeneous structures, scattering losses can dominate the overall loss. As the GPR's frequency decreases, the physical size of the structures which result in scattering losses increases. Following this trend, reducing the GPR frequency will in effect reduce the overall scattering losses. This makes lower radar frequencies more desirable for highly variable structures.

Even if the soil scattering loss is constant regardless of absorption losses, the significance of the scattering loss will increase with lower absorption losses. But at some point, scattering losses will be a significant fraction of the extinction cross-section, and at this point, the materials bulk electrical properties are no longer sufficient for characterizing radar attenuation. Care must be taken when extrapolating losses to long distances, especially with significant changes in the absorption cross-section.

VII. CONCLUSION AND RECOMMENDATIONS

Electromagnetic remote sensing techniques provide a means to detect changes in the electromagnetic properties of a material which are usually manifested as a gradient in their characteristic impedance. A change in material composition can be a result of an interface between two materials but can also be due to variations in density, water saturation, and salinity. This variability is observed both with depth but also laterally. The probability of detecting the variations in the material's properties increases as the contrast between the two materials increases. Under hydrostatic equilibrium, the capillary rise

IEEE Access

R. M. Beauchamp *et al.*: Can Airborne GPRs Explore Groundwater in Hyper-Arid Regions?

from the water table (recall that the water table is at 100% saturation) is expected to be less than 1 m where the top of this rise is at approximately the minimum water saturation of the material. With this transition depth and at frequencies of interest, the top of the water table should provide an ideal interface for radar detection provided signal attenuation and clutter are overcome.

Based on a review of both published field measurements and the experiment results presented here, soil characteristics are found to be highly variable with depth, geographic location, and time. The signal attenuation due to absorption is largely dominated by the conductivity of the subsurface. Low frequency (or DC) conductivity estimates are representative of the conductivities at the radar frequencies considered here. From a survey of existing soil measurements of permittivity and conductivity, a relative permittivity between 3 and 30 and a conductivity between 10^{-4} and 1 S/m is expected. As the radar frequency decreases, the conductivity loss dominates over dielectric losses. For materials that meet the ''good conductor'' criterion, the attenuation shows a $\sqrt{f}$ dependence. It is noted that the material's bulk conductivity is largely dominated by the grain size (which relates to the minimum amount of pore fluid within the structure for a ''dry'' state) and pore fluid conductivity. Dissolved solids (salts) increase the pore fluid conductivity and for most materials, the conductivity of the pore fluid largely dominates the bulk properties of the subsurface. Variation of the water content and temperature can exhibit a significant change in the electrical resistance of the subsurface.

For deep radar sounding in soils, it is clear that low frequencies are desired to enable detection at greater depths. Using GPR at frequencies on the order of 10 MHz in sand dunes or unconsolidated material, depths greater than 100 m have been reported. The practical limits on how low of a frequency to use is a function of required range resolution for the application and the ability (or suitability) of the antenna system to be used.

In this work, we reviewed the electromagnetic characteristics of soil and subsurface materials that are expected to be found in hyper-arid regions for the purposes of remote sensing exploration of water. As such, the depths over which a system can detect water was fundamental to this study and has given us two physical ''parameters'': 1) the maximum sounding depth, and 2) the minimum near-surface detection depth. With the goal of realizing a system to achieve the goal of detecting subsurface water, additional constraints are placed on the practicality of building and operating such a system on an airborne platform. There are practical limitations on the antenna size and structure for use with an aircraft, as well as operating altitudes for both safety and performance. This practical aspect leads to two additional ''parameters'': 3) survey altitude, and 4) antenna size. The radar's center frequency and its operational bandwidth are included within these parameters but their selection is a direct result of their impact on this parameter space (they are the independent

variables to tune with the cost function derived from these parameters). Consider the parameter trade space:

- A narrow antenna beam width is desired to reduce the impact of clutter for the subsurface depths of interest (impacts sounding depth, antenna size, and survey altitude).
- To achieve narrow antenna beam width (for a fixed size aperture), higher frequencies are required (impacts sounding depth and antenna size).
- For deep subsurface sounding, lower frequencies are desired to reduce attenuation effects (impacts sounding depth and antenna size).
- Higher bandwidth signals are desired to resolve small features (i.e., minimize ΔR) (impacts near-surface detection and survey altitude).
- As the bandwidth increases, higher frequencies are typically required (impacts near-surface detection, sounding depth, and antenna size).

The GPR penetration depth is subject to a number of environmental and system variables. The variability of subsurface properties in time and space requires a probabilistic evaluation of performance. Conductivity can vary multiple orders of magnitude and permittivity can vary an order of magnitude (depending on subsurface conditions). As the penetration depth increase, the effects of approximations for estimating attenuation can be significant (i.e., the depth uncertainty is proportional to the input uncertainty). With 1 to 10 MHz radar systems at ''very-high'' and ''unusually high'' resistivity, which exhibit low loss ($A_1 = 0.1$ dB/m), sounding depths are potentially in excess of 500 m for high SNR/SCR systems. Again, the scattering losses may be significant for low absorption loss conditions and have a significant impact on penetration depth. Sounding depths of up to 100 m are feasible for high resistivity materials. GPR in sand dunes and Quaternary unconsolidated materials have demonstrated penetration up to 100 m and more. With a modest increase in water saturation or pore fluid salinity, the penetration depths likely will decrease to tens of meters.

The discussion and analysis throughout this paper are presented to help answer the title's question ''Can airborne ground penetrating radars study groundwater tables in hyper-arid regions?'' The short answer is a qualified ''yes''. With low radar frequencies (on the order of 10 MHz or less), adequate ground clutter rejection, and medium or higher vadose zone soil resistivity, the detection of water table depths of 50 meters and beyond are feasible. For observations in dry sand dunes and dry unconsolidated materials, the detection depths likely extend to 100-200 meters with ideal (very low loss) conditions.

R. M. Beauchamp *et al.*: Can Airborne GPRs Explore Groundwater in Hyper-Arid Regions?

IEEE *Access*

REFERENCES

[1] Y. Fan, H. Li, and G. Miguez-Macho, "Global patterns of groundwater table depth," *Science*, vol. 339, no. 6122, pp. 940–943, 2013. [Online]. Available: http://science.sciencemag.org/content/339/6122/940

[2] S. Siebert, J. Burke, J. M. Faures, K. Frenken, J. Hoogeveen, P. Döll, and F. T. Portmann, "Groundwater use for irrigation—A global inventory," *Hydrol. Earth Syst. Sci.*, vol. 14, no. 10, pp. 1863–1880, 2010.

[3] H. C. J. Godfray *et al.*, "Food security: The challenge of feeding 9 billion people," *Science*, vol. 327, no. 5967, pp. 812–818, 2010.

[4] W. V. Reid *et al.*, "Earth system science for global sustainability: Grand challenges," *Science*, vol. 330, no. 6006, pp. 916–917, 2010.

[5] S. Banwart, "Save our soils," *Nature*, vol. 474, no. 7350, pp. 151–152, 2011.

[6] T. Gleeson, K. M. Befus, S. Jasechko, E. Luijendijk, and M. B. Cardenas, "The global volume and distribution of modern groundwater," *Nature Geosci.*, vol. 9, pp. 1–15, Nov. 2015. [Online]. Available: http://www.nature.com/ngeo/journal/vaop/ncurrent/full/ngeo2590.html

[7] A. Binley *et al.*, "The emergence of hydrogeophysics for improved understanding of subsurface processes over multiple scales," *Water Resour. Res.*, vol. 51, no. 6, pp. 3837–3866, 2015.

[8] E. Chaussard, P. Milillo, R. Bürgmann, D. Perissin, E. J. Fielding, and B. Baker, "Remote sensing of ground deformation for monitoring groundwater management practices: Application to the Santa Clara Valley during the 2012–2015 California drought," *J. Geophys. Res., Solid Earth*, vol. 122, no. 10, pp. 8566–8582, 2017, doi: 10.1002/2017JB014676.

[9] M. Manga, "On the timescales characterizing groundwater discharge at springs," *J. Hydrol.*, vol. 219, nos. 1–2, pp. 56–69, 1999.

[10] J. O. Skøien, G. Blöschl, and A. W. Western, "Characteristic space scales and timescales in hydrology," *Water Resour. Res.*, vol. 39, no. 10, pp. SWC 11-1–SWC 11-19, 2003, doi: 10.1029/2002WR001736.

[11] J. R. Nimmo, R. W. Healy, and D. A. Stonestrom, "Aquifer recharge," in *Encyclopedia of Hydrological Science: Part 13. Groundwater*, vol. 4, M. G. Anderson and J. Bear, Eds. Chichester, U.K.: Wiley, 2005, pp. 2229–2246. [Online]. Available: http://www.mrw.interscience.wiley.com/ehs/articles/hsa161a/frame.html, doi: 10.1002/0470848944.hsa161a.

[12] *SMAP Handbook*, Jet Propuls. Lab., Pasadena, CA, USA, 2014.

[13] P. Castellazzi *et al.*, "Groundwater depletion in Central Mexico: Use of GRACE and InSAR to support water resources management," *Water Resour. Res.*, vol. 52, no. 8, pp. 5985–6003, 2016.

[14] D. H. R. Hellwig, "Evaporation of water from sand, 4: The influence of the depth of the water-table and the particle size distribution of the sand," *J. Hydrol.*, vol. 18, nos. 3–4, pp. 317–327, 1973.

[15] F. Ciocca, I. Lunati, and M. B. Parlange, "Effects of the water retention curve on evaporation from arid soils," *Geophys. Res. Lett.*, vol. 41, no. 9, pp. 3110–3116, 2014.

[16] I. Mughal, K. Z. Jadoon, P. M. Mai, S. Al-Mashharawi, and T. M. Missimer, "Experimental measurement of diffusive extinction depth and soil moisture gradients in a dune sand aquifer in Western Saudi Arabia: Assessment of evaporation loss for design of an MAR system," *Water*, vol. 7, no. 12, pp. 6967–6982, 2015.

[17] O. M. Lopez, K. Z. Jadoon, and T. M. Missimer, "Method of relating grain size distribution to hydraulic conductivity in dune sands to assist in assessing managed aquifer recharge projects: Wadi Khulays dune field, Western Saudi Arabia," *Water*, vol. 7, no. 11, pp. 6411–6426, 2015.

[18] Q. Feng, G. D. Cheng, and K. N. Endo, "Water content variations and respective ecosystems of sandy land in China," *Environ. Geol.*, vol. 40, no. 9, pp. 1075–1083, 2001.

[19] E. Gloaguen, M. Chouteau, D. Marcotte, and R. Chapuis, "Estimation of hydraulic conductivity of an unconfined aquifer using cokriging of GPR and hydrostratigraphic data," *J. Appl. Geophys.*, vol. 47, no. 2, pp. 135–152, 2001.

[20] R. H. Brooks and A. T. Corey, *Hydraulic Properties of Porous Media,' Hydrology Papers*, vol. 3. Fort Collins, CO, USA: Colorado State Univ., 1964, p. 27.

[21] P. M. Reppert, F. D. Morgan, and M. N. Toksöz, "Dielectric constant determination using ground-penetrating radar reflection coefficients," *J. Appl. Geophys.*, vol. 43, nos. 2–4, pp. 189–197, 2000.

[22] K. Takahashi, J. Igel, H. Preetz, and S. Kuroda, "Basics and application of ground-penetrating radar as a tool for monitoring irrigation process," in *Problems, Perspectives and Challenges of Agricultural Water Management*, M. Kumar, Eds. Rijeka, Croatia: InTech, 2012. [Online]. Available: http://www.intechopen.com/books/problems-perspectives-and-challenges-of-agricultural-water-management/basics-and-application-of-ground-penetrating-radar-as-a-tool-for-monitoring-irrigation-process

[23] A. Revil, "Effective conductivity and permittivity of unsaturated porous materials in the frequency range 1 mHz–1 GHz," *Water Resour. Res.*, vol. 49, no. 1, pp. 306–327, 2013.

[24] T. M. Levitskaya and B. K. Sternberg, "Polarization processes in rocks: 1. Complex dielectric permittivity method," *Radio Sci.*, vol. 31, no. 4, p. 781, 1996.

[25] G. Hamann and J. Tronicke, "Global inversion of GPR traveltimes to assess uncertainties in CMP velocity models," *Near Surf. Geophys.*, vol. 12, no. 4, pp. 505–514, 2014.

[26] B. K. Sternberg and T. M. Levitskaya, "Electrical parameters of soils in the frequency range from 1 kHz to 1 GHz, using lumped-circuit methods," *Radio Sci.*, vol. 36, no. 4, pp. 709–719, 2001.

[27] R. E. Grimm, E. Heggy, S. M. Clifford, C. L. Dinwiddie, R. McGinnis, and D. Farrell, "Absorption and scattering in ground-penetrating radar: Analysis of the Bishop Tuff," *J. Geophys. Res. E, Planets*, vol. 111, no. E6, pp. 1–15, 2006.

[28] E. Heggy, S. M. Clifford, R. E. Grimm, C. L. Dinwiddie, J. A. Stamatakos, and S. H. Gonzalez, "Low-frequency radar sounding investigations of the North Amargosa Desert, Nevada: A potential analog of conductive subsurface environments on mars," *J. Geophys. Res. E, Planets*, vol. 111, no. 6, pp. 1–11, 2006.

[29] J. Francke and D. Tatum, "Regional variability of ground penetrating radar response—A case study from the dune fields of the United Arab Emirates (UAE)," in *Proc. 15th Int. Conf. Ground Penetrating Radar (GPR)*, Jul. 2014, pp. 998–1005.

[30] R. J. Knight and A. Nur, "The dielectric constant of sandstones, 60 kHz to 4 MHz," *Geophysics*, vol. 52, no. 5, pp. 644–654, 1987.

[31] J. D. McNeill, "Electrical conductivity of soils and rocks," Geonics Ltd., Mississauga, ON, Canada, Tech. Note TN-5, 1980.

[32] R. Knight and A. Abad, "Rock/water interaction in dielectric properties: Experiments with hydrophobic sandstones," *Geophysics*, vol. 60, no. 2, pp. 431–436, 1995.

[33] S. A. Al Hagrey and C. Müller, "GPR study of pore water content and salinity in sand," *Geophys. Prospecting*, vol. 48, no. 1, pp. 63–85, 2000.

[34] J. D. Irving and R. J. Knight, "Removal of wavelet dispersion from ground-penetrating radar data," *Geophysics*, vol. 68, no. 3, pp. 960–970, 2003.

[35] *IEEE Guide for Measuring Earth Resistivity, Ground Impedance, and Earth Surface Potentials of a Grounding System—Redline*, IEEE Standard 81-2012, Substations Committee, Dec. 2012.

[36] K. Norsangsri and T. Kulworawanichpong, "Earth resistivity estimation based on satellite imaging techniques," *WSEAS Trans. Syst.*, vol. 8, no. 9, pp. 1061–1071, 2009.

[37] A. A. Garrouch and M. M. Sharma, "The Influence of clay content, salinity, stress, and wettability on the dielectric properties of brine-saturated rocks: 10 Hz to 10 MHz," *Geophysics*, vol. 59, no. 6, pp. 909–917, 1994.

[38] A. R. von Hippel, Ed., *Dielectric Materials and Applications*. Cambridge, MA, USA: MIT Press, 1954.

[39] P. A. Patil *et al.*, "Electrical resistivity and permittivity measurements of oil base muds in the frequency range from 1 MHz to 100 MHz," *SPE Drilling Completion*, vol. 25, no. 3, pp. 380–390, 2010.

[40] J. W. Crispin and A. L. Maffett, "Radar cross-section estimation for complex shapes," *Proc. IEEE*, vol. JPROC-53, no. 8, pp. 972–982, Aug. 1965.

[41] R. Ross, "Radar cross section of rectangular flat plates as a function of aspect angle," *IEEE Trans. Antennas Propag.*, vol. TAP-14, no. 3, pp. 329–335, May 1966.

[42] G. Brown, "The average impulse response of a rough surface and its applications," *IEEE Trans. Antennas Propag.*, vol. TAP-25, no. 1, pp. 67–74, Jan. 1977.

[43] T. Hagfors, "Backscattering from an undulating surface with applications to radar returns from the Moon," *J. Geophys. Res.*, vol. 69, no. 18, pp. 3779–3784, 1964.

IEEE Access

R. M. Beauchamp *et al.*: Can Airborne GPRs Explore Groundwater in Hyper-Arid Regions?

[44] W. Dierking, "Quantitative roughness characterization of geological surfaces and implications for radar signature analysis," *IEEE Trans. Geosci. Remote Sens.*, vol. 37, no. 5, pp. 2397–2412, Sep. 1999.

[45] J. T. Johnson, K. F. Warnick, and P. Xu, "On the geometrical optics (Hagfors' law) and physical optics approximations for scattering from exponentially correlated surfaces," *IEEE Trans. Geosci. Remote Sens.*, vol. 45, no. 8, pp. 2619–2629, Aug. 2007.

[46] (Feb. 20, 2018). *Geotomo Software*. [Online]. Available: http://www.geotomosoft.com/index.php

[47] N. Malik, A. A. Al-Arainy, M. I. Qureshi, and M. S. Anam, "Measurements of earth resistivity in different parts of Saudi Arabia for grounding installations," in *Proc. 7th Saudi Eng. Conf.* Riyadh, Saudi: King Saud Univ., 2007.

[48] L. J. Chu, "Physical limitations of omni-directional antennas," *J. Appl. Phys.*, vol. 19, no. 12, pp. 1163–1175, 1948.

[49] G. F. Stickley, D. A. Noon, M. Cherniakov, and I. D. Longstaff, "Gated stepped-frequency ground penetrating radar," *J. Appl. Geophys.*, vol. 43, pp. 259–269, Mar. 2000.

[50] T. T. Wu and R. W. P. King, "The cylindrical antenna with nonreflecting resistive loading," *IEEE Trans. Antennas Propag.*, vol. TAP-13, no. 3, pp. 369–373, May 1965.

[51] V. Ciarletti, A. Le Gall, J. J. Berthelier, C. Corbel, F. Dolon, and F. Ney, "Bistatic deep soundings with the HF GPR TAPIR in the Egyptian white desert," in *Proc. 37th Lunar Planetary Sci.*, 2006.

[52] A. L. Gall *et al.*, "An imaging HF GPR using stationary antennas: Experimental validation over the antarctic ice sheet," *IEEE Trans. Geosci. Remote Sens.*, vol. 46, no. 12, pp. 3975–3986, Dec. 2008.

[53] V. Ciarletti *et al.*, "Bistatic sounding of the deep subsurface with a ground penetrating radar—Experimental validation," *Planet. Space Sci.*, vol. 117, pp. 177–183, Nov. 2015, doi: 10.1016/j.pss.2015.06.008.

[54] R. E. Grimm, D. E. Stillman, C. L. Dinwiddie, R. N. McGinnis, and S. K. Sandberg "On conductive ground: Analysis of 'bistatic sounding of the deep subsurface with ground penetrating radar—Experimental validation' by V. Ciarletti *et al.*," *Planetary Space Sci.*, vol. 139, pp. 51–56, Aug. 2017, doi: 10.1016/j.pss.2017.02.010.

[55] J. Mouginot, E. Rignot, Y. Gim, D. Kirchner, and E. Le Meur, "Low-frequency radar sounding of ice in East Antarctica and southern Greenland," *Ann. Glaciol.*, vol. 55, no. 67, pp. 138–146, 2014.

[56] D. G. Smith and H. M. Jol, "Ground penetrating radar: Antenna frequencies and maximum probable depths of penetration in quaternary sediments," *J. Appl. Geophys.*, vol. 33, no. 1, pp. 93–100, 1995.

[57] N. M. Vriend, M. L. Hunt, and R. W. Clayton, "Sedimentary structure of large sand dunes: Examples from Dumont and Eureka dunes, California," *Geophys. J. Int.*, vol. 190, no. 2, pp. 981–992, 2012.

[58] Z. Harari, "Ground-penetrating radar (GPR) for imaging stratigraphic features and groundwater in sand dunes," *J. Appl. Geophys.*, vol. 36, no. 1, pp. 43–52, 1996.

[59] J. Francke and V. Utsi, "Advances in long-range GPR systems and their applications to mineral exploration, geotechnical and static correction problems," *First Break*, vol. 27, no. 7, pp. 85–93, 2009.

[60] J. Francke, "The application of long-range GPR for seismic static corrections," in *Proc. 16th Int. Conf. Ground Penetrating Radar (GPR)*, Jun. 2016, pp. 1–6.

DARMINDRA D. ARUMUGAM received the B.S. and M.S. degrees in electrical engineering from the University of Texas at Arlington and the Ph.D. degree in electrical and computer engineering from Carnegie Mellon University, with focus on applied physics. He is currently a Senior Research Technologist and an Applied Physics Program Manager with the Jet Propulsion Laboratory, California Institute of Technology. He has authored over 50 articles in IEEE journals and conferences. His research in applied electromagnetics presently focuses on radio propagation and scattering, radar imaging and sounding systems, localization systems, ionospheric/plasma science, quasistatic fields, and wireless power transfer. He leads a few NASA/JPL projects/missions as a Principal Investigator, and a technical research group. His research has appeared in numerous IEEE journals, and both national and international media/press such as *Newsweek* and *Popular Mechanics*. He has received numerous awards, including the Mariner Award (2014), Voyager Award (2015), Lew Allen Award (2016), and a few IEEE conference awards.

MARIKO S. BURGIN (S'09–M'14–SM'17) received the M.S. degree in electrical engineering and information technology from the Swiss Federal Institute of Technology, Zurich, Switzerland, in 2008, and the M.S. and Ph.D. degrees in electrical engineering from the Radiation Laboratory, University of Michigan, Ann Arbor, MI, USA, in 2011 and 2014. From 2014 to 2015, she was a Post-Doctoral Scholar with the Water and Carbon Cycles Group, Jet Propulsion Laboratory (JPL), California Institute of Technology, Pasadena, CA, USA. She is currently a Scientist with JPL and a Visiting Associate Researcher with the University of California, Los Angeles. Her scientific research focuses on electromagnetic modeling and retrieval algorithm development for active and passive microwave remote sensing applications. She serves on the SMAP Science Team and is the recipient of two NASA Group Achievement Awards. She is a Senior Member of the IEEE Geoscience and Remote Sensing Society (GRSS), the IEEE Women in Engineering, and the IEEE Young Professionals. She is the Vice-Chair of the IEEE Metropolitan Los Angeles GRSS Chapter and a member-elect of the IEEE GRSS Administrative Committee (AdCom).

JACK D. BUSH received the B.S. and M.S. degrees in electrical engineering from the Georgia Institute of Technology, Atlanta, GA, USA, in 2015 and 2017, respectively. In 2017, he joined the Suborbital Radar Science and Engineering Group, Jet Propulsion Laboratory, California Institute of Technology.

ROBERT M. BEAUCHAMP received the B.S. degree from the University of Massachusetts Amherst, Amherst, MA, USA, the M.S. degree from Northeastern University, Boston, MA, USA, and the Ph.D. degree from Colorado State University, Fort Collins, CO, USA, all in electrical engineering. He is currently a Radar Systems Engineer with the Jet Propulsion Laboratory, California Institute of Technology. His research interests include radar remote sensing and signal processing methods to quantify geophysical properties.

ALA KHAZENDAR received the Ph.D. degree in geophysical sciences from the Universit Libre de Bruxelles, Belgium. He is currently a Scientist with the Jet Propulsion Laboratory, California Institute of Technology, Pasadena, CA, USA, where he focuses on the remote sensing and numerical modeling of ice shelves and ice sheets and their interactions with the ocean.

R. M. Beauchamp *et al.*: Can Airborne GPRs Explore Groundwater in Hyper-Arid Regions?

IEEE *Access*

YONGGYU GIM received the B.S. and M.S. degrees from Seoul National University, and the Ph.D. degree from the University of Maryland College Park, all in physics. He has been with the Radar Science and Engineering Section, Jet Propulsion Laboratory, California Institute of Technology, since 2001. He is currently a science Co-Investigator with the Europa Radar Science Team and also leads U.S. radar development for European Jupiter mission. His current interests include radar sounding technology developments and mission formulations to explore small icy bodies in the solar system.

MAJED ALMALKI received the M.Sc. degree in geophysics with King Saud University and the Ph.D. degree with Curtin University, Perth. He has been with the King Abdulaziz City for Science and Technology (KACST) since 2002. During this period, he has been involved in seismic processing and conducts research related to high resolution of seismic data, NDT, radar, tomography, borehole seismic, FWS, dispersion analysis, and seismology. He has been the Manager of the National Center for Oil and Gas Technology, KACST, since 2014.

YASIR A. ALMUTAIRI received the bachelor's and master's degree in geophysics from King Saud University, Riyadh, Saudi Arabia, in 2008 and 2015, respectively. He has been a Geophysicist with the Oil and Gas Research Institute, King Abdulaziz City for Science and Technology, Riyadh, since 2009. His research interest is in the area of ground penetrating radar.

SULTAN ALMORQI received the bachelor's and Ph.D. degrees in electrical engineering from Herriot Watt University, Edinburgh, Scotland. He was with the King Abdulaziz City for Science and Technology (KACST), as the Director of National Center for Sensors Technology and Defense Systems. He also served as the Deputy Director for scientific affairs with the Advanced Sensors for Electronics Defense Center and as a Radar Systems Engineer with KACST for several projects. He is currently a President and a Chief Executive Officer for Saudi Defense Electronics Company. He has published extensively on folded waveguide resonators and has published and co-published 26 papers. He is a member of the IEEE Society for Electrical and Electronic Engineers, the Communications Society of America, the Saudi Council of Engineers, a member of the Board of Directors of the Saudi Telecommunications Engineering and the Chairman of Scientific and Cultural Division in Saudi Telecommunications Society. He was elected as the President of Saudi AOC Chapter in 2013. In 2015, he was appointed to be the Co-Director for the Microwave Sensors Technology Joint Center, KACST, and the University of Michigan, also he was the Principal Investigator of Radar Exploration of Desert Aquifers which is joint project between KACST and the California Institute of Technology/Jet Propulsion Laboratory. He also attended the Program for Leadership Development with the Harvard Business School, an alternative to executive MBA.

ALI A. ALSAMA received the bachelor's and master's degrees in geophysics from King Saud University, Riyadh, Saudi Arabia, in 2006 and 2012, respectively. He has been a Geophysicist with the Oil and Gas Research Institute, King Abdulaziz City for Science and Technology, since 2007. His research interest is in the area of geoelectrical and magnetic methods.

ABDULRAHMAN G. ALANEZI received the bachelor's and master's degrees in geophysics from King Saud University, Riyadh, Saudi Arabia, in 2007 and 2012, respectively. He has been a Geophysicist with the Oil and Gas Research Institute, King Abdulaziz City for Science and Technology, since 2007. His research interest is in the area of seismic exploration with emphasis on seismic inversion, velocity model building, and MASW.

● ● ●